



저작자표시-비영리-변경금지 2.0 대한민국

이용자는 아래의 조건을 따르는 경우에 한하여 자유롭게

- 이 저작물을 복제, 배포, 전송, 전시, 공연 및 방송할 수 있습니다.

다음과 같은 조건을 따라야 합니다:



저작자표시. 귀하는 원저작자를 표시하여야 합니다.



비영리. 귀하는 이 저작물을 영리 목적으로 이용할 수 없습니다.



변경금지. 귀하는 이 저작물을 개작, 변형 또는 가공할 수 없습니다.

- 귀하는, 이 저작물의 재이용이나 배포의 경우, 이 저작물에 적용된 이용허락조건을 명확하게 나타내어야 합니다.
- 저작권자로부터 별도의 허가를 받으면 이러한 조건들은 적용되지 않습니다.

저작권법에 따른 이용자의 권리는 위의 내용에 의하여 영향을 받지 않습니다.

이것은 [이용허락규약\(Legal Code\)](#)을 이해하기 쉽게 요약한 것입니다.

[Disclaimer](#)

공학박사학위논문

파단 기반 미세 변형 감지 센서의 최적화 및 안정화 연구

Study on optimization and stabilization of crack-based
strain and pressure sensors

2019 년 2 월

서울대학교 대학원

기계항공공학부

이 태 민

Abstract

In this thesis, we present multilayered structural crack-based sensory systems with different fracture characteristics of metal thin films and high durable crack-based sensory systems that use the heat deformation properties of the polymer.

First, we propose a new type of the crack-based sensory systems by using the different crack-forming characteristics of metal thin films against an applied tensile force. The cracks are induced on the ductile conductive thin films by attaching the brittle metal thin films. The crack-induced conductive thin film shows dramatic resistance change with the applied strain. In addition, the adhesive oxide thin film is deposited between the brittle metal thin films and the substrates to stabilize the crack-based sensory system in cyclic loading and unloading.

Next, we present the transparent crack-based sensory systems with brittle transparent conductive oxide films. An Indium-Tin Oxide layer with the high transparency at visible light wavelengths, high conductivity, and appropriate brittleness to form the cracks with small applied strain is suitable material for the transparent crack-based sensory systems. Therefore, we fabricate the transparent crack-based sensory systems by simply depositing the Indium-Tin Oxide layer on the polymer substrates with a sputter. After the deposition, the polymer substrates

are stretched to form cracks on the Indium-Tin Oxide films. The proposed transparent sensory systems have high sensitivity to stretching, high transmittance to visible light, and stability against repeated stretching. In addition, we have developed the transparent crack-based sensory systems as pressure sensors. The proposed transparent pressure sensors have high transmittance to visible light, wide range of pressure measuring, and high sensitivity to pressure.

Finally, we propose the stabilized crack sensory systems through polymeric encapsulation methods. In case of the conventional crack sensory systems, the surface of the metal thin films is directly exposed to the outside, which is vulnerable to harsh, external environments. Thus, in this study, the degree of durability and stability of the crack sensory systems against moisture, chemical reactions, and scratches is improved by encapsulating the systems with strong chemical resistance polymers.

Key Words : Multi-layered metal thin film, cracks, strain sensor, pressure sensor, transparent sensor, encapsulation,

Student Number: 2014-31037

Contents

Abstract	i
List of Figures	v
Chapter 1. Introduction	
1-1. Introduction	1
1-2. References	6
Chapter 2. Brittle thin layer induced diverse conductive materials layered crack-based sensory systems	
2-1. Crack-based strain sensory system with diverse metal films by inserting brittle thin metal layer	10
2-1-1. Introduction	10
2-1-2. Experimental	12
2-1-3. Results and Discussion	13
2-1-3-1. Composition of metal layered crack sensors	13
2-1-3-2. Measurements of the performance of the metal layered Crack sensors	21
2-1-3-3. Detecting the hands motion by using metal layered crack sensors	33
2-1-4. Summary	36
2-1-5. References	37
2-2. Crack-induced brittle transparent conductive materials sensory	

systems.....	40
2-2-1. Introduction	40
2-2-2. Experimental	42
2-2-3. Results and Discussion	43
2-2-3-1. Mechanism of the transparent ITO crack sensory systems.....	43
2-2-3-2. The pressure sensing with bended crack based sensors	55
2-2-3-3. Hand motions sensing with bended crack based sensors	61
2-2-4. Summary	63
2-2-5. References.....	64
Chapter 3. Stabilized crack-based sensory systems with encapsulation	
3-1. Crack sensors encapsulation.....	67
3-1-1. Introduction	67
3-1-2. Experimental	69
3-1-3. Results and Discussion	73
3-1-3-1. Polyimide encapsulation.....	73
3-1-3-2. FEP encapsulation.....	88
3-1-4. Summary	98
3-1-5. References.....	99
Acknowledgement	103
국문초록	104

List of Figures

- Figure 2-1. Schematic images of a metal layered crack sensor.** (a) The image of a metal layered crack sensor with Cr and MoO₃ interlayers. (b) The real image of metal layered crack sensors. The sensors on the left side is an Au layered crack sensor. The sensors in the center are Ag layered crack sensors. The sensors on the right side are Pt layered crack sensors.
- Figure 2-2 The SEM image of the conductive materials deposited on the PET substrates after applying strain of 2%.** (a) Au deposited PET substrates after stretched strain of 2%. (b) Ag deposited PET substrates after stretched strain of 2%. (c) Pt deposited PET substrates after stretched strain of 2%.
- Figure 2-3. The illustration of the cracks on the sensor before stretching (left), and the cracks after stretching (right).** The cracks on the conductive metal layer are induced by the cracks on the interlayer underneath the metal layer (the inserted image).
- Figure 2-4. SEM images of the metal layered crack sensors.** (a) The SEM image of Cr (30 nm) and MoO₃ (5 nm) on the PET substrate after strain of 2%. The inserted image is a magnified image of a crack on the Cr and MoO₃ layered PET substrate. (b) The SEM image of an Au layered crack sensor after strain of 2%. The inserted image is a magnified image of a crack on the Au layered crack sensor. (c) The SEM image of an Ag layered crack sensor after strain of 2%. The inserted image is a magnified image of a crack on the Ag layered crack sensor. (d) The SEM image of a Pt layered crack sensor after strain of 2%. The inserted image is a magnified image of a crack on the Pt layered crack sensor.
- Figure 2-5. The SEM image of the conductive materials deposited on the MoO₃/PET substrates.** (a) Au deposited MoO₃/PET substrates. (b) Ag deposited MoO₃/PET substrates. (c) Pt deposited MoO₃/PET substrates.
- Figure 2-6. The Performance graph of the metal layered crack sensors.** (a) The graph of the Au layered crack sensors' normalized

resistance variance versus strain of 2% in 10 cyclic tests. **(b)** The graph of the Ag layered crack sensors normalized resistance variance versus strain of 2% in 10 cyclic tests. **(c)** The graph of the Pt layered crack sensors normalized resistance variance versus strain of 2% in 10 cyclic tests. **(d)** The average and standard deviations of the 5 different Au layered crack sensors with hysteresis tests. Red dots show the unloading process and black dots show the loading process. **(e)** The average and standard deviations of the 5 different Ag layered crack sensors with hysteresis tests. Red dots show the unloading process and black dots show the loading process. **(f)** The average and standard deviations of the 5 different Pt layered crack sensors with hysteresis tests. Red dots show the unloading process and black dots show the loading process.

Figure 2-7. The graph of comparison between the conductive materials deposited on the PET substrates and the metal layered crack sensors with strain of 2% in a 10 time cyclic test. (a) The graph of comparison between the Au deposited on the PET substrates (red line) and the Au layered crack sensor (black line). (b) The graph of comparison between the Ag deposited on the PET substrates (blue line) and the Ag layered crack sensor (black line). (c) The graph of comparison between the Pt deposited on the PET substrates (blue line) and the Pt layered crack sensor (black line).

Figure 2-8. The SEM image of the conductive materials deposited on the PUA/PET substrates. (a) Au deposited PUA/PET substrates. (b) Ag deposited PUA/PET substrates.

Figure 2-9. The graph of comparison between the conductive materials deposited on the PUA/PET substrates and the metal layered crack sensors with strain of 2% in a 10 time cyclic test. (a) The graph of comparison between the Au deposited on the PUA/PET substrates (red line) and the Au layered crack sensor (black line). (b) The Au deposited on the PUA/PET substrate graph of the normalized resistance variance versus strain of 2%. (c) The graph of comparison between the Ag deposited on the PUA/PET substrates (red line) and the Ag layered crack sensor (black line). (d) The Ag deposited on the PUA/PET substrate graph of the normalized resistance variance versus strain of 2%.

- Figure 2-10.** The graph for reversible tests with the metal layered crack sensors with various strains. The given strain on the sensor are 0.5% (blue line), 1.0% (red line), and 2.0% (black line). (a) The reversible test of Au layered crack sensor. (b) The reversible test of Ag layered crack sensor. (c) The reversible test of Pt layered crack sensor.
- Figure 2-11.** A marathon test of the conductive material layered sensors by repeating loading/unloading process about 5,000 cycles at strain from 0% to 2%. (a) A final normalized resistance of a marathon test at a certain period with an Au layered crack sensor, (b) an Ag layered crack sensor and (c) a Pt layered crack sensor
- Figure 2-12.** A marathon test of a Pt layered sensors without MoO₃ layer by repeating loading/unloading process about 650 cycles at strain from 0% to 2%.
- Figure 2-13.** Detecting the hands motion by Au metal layered crack sensors on the knuckles of the index and ring fingers (a) with the hand spread out, (b) with the hand clenched, (c) with the index finger spread out while the ring finger is clenched. (d) The graphs represent the Au metal layered crack sensors' normalized resistance variations due to the hand movement. The images on the left and right are the sensors on the index finger, and the ring finger, respectively, while (d) the hand spread out, (e) the hand clenched, and (f) the index finger spread out while the ring finger is clenched.
- Figure 2-14.** Schematic images of a transparent crack sensor. (a) The image of crack opening while cracks are generated with cyclic strain from 0% to 2%. (b) FESEM image in which the cracks on the sensor are parallel to each other. (c) The transparent ITO crack sensor shows clear view of background behind.
- Figure 2-15.** A graph of transmittance versus light wavelength through the crack sensor.
- Figure 2-16.** SEM images of crack opening. (a) SEM image of the crack on the ITO layer with no external tension. (b) SEM image of the

crack on the ITO layer with strain of 2%.

- Figure 2-17.** The graph for loading/unloading tests with the ITO mechanical crack-based sensor with various strains.
- Figure 2-18.** **The variations of the performance of the ITO crack sensor with enhanced strain of 2%.** (a) The graph of normalized resistance variance versus strain of 2% in a 10time cyclic test. (b) The standard deviation and the average over 10 different samples in the hysteresis test of the ITO crack sensor. Red and black dots show unloading and loading statuses, respectively.
- Figure 2-19.** **The graph for reversible tests with the ITO mechanical crack-based sensor with various strains.** The given strains on the sensor are 0.5%, 1.0%, 1.5% and 2%.
- Figure 2-20.** The graph of the ITO crack sensor response time.
- Figure 2-21.** Images on the top show the ITO crack sensors on the PET film (on the left) and on the PDMS film (on the right) with their cross-sectional schematic illustrations below each image.
- Figure 2-22.** The graph of strain – stress curve of the PET substrate strain from 0% to 10%.
- Figure 2-23.** The gauge factor of the ITO crack sensors with different ITO thickness. (65 nm, 130 nm, 600 nm)
- Figure 2-24.** **The transparent pressure sensor based on the ITO crack sensor mechanism.** (a) The schematic image of the 4 by 4 ITO pressure sensor pixel matrix. The image on the bottom shows the visualized stress data of a single pixel of the pressure sensor. (b) The graph of normalized resistance versus pressure ranging from 0 to 70 kPa. The slope of the normalized resistance versus pressure from 0 to 30 kPa is 0.21 kPa^{-1} , and pressure from 30 to 70 kPa is 1.91 kPa^{-1} .
- Figure 2-25.** **A single crack-sensor pressure detecting.** (a) Photo image of acrylic frame for strain sensing mode. (b) Photo image of acrylic frame for pressure sensing mode. (c) Resistance change on the strain sensing mode with vertical pressure (0.15 kPa). (d)

Resistance change on the pressure sensing mode with vertical pressure (0.15 kPa).

- Figure 2-26. Fabrication of the multi-pixel array pressure sensor.** (a) ITO layer is deposited by a sputter on a PET substrate through a shadow mask. (b) Thin Ag metal layer (about 13 nm) is deposited on the ITO layer coated with the PET film by a thermal evaporator through an electrode path shadow mask. (c) A PDMS with 4 by 4 square hole is attached on the ITO layer coated with the PET film. (d) The edges of each pixel facing each other were cut.
- Figure 2-27. The multi-array based ITO pressure crack sensor** (a) The photo image of the transparent pressure sensor multi-array on a display panel. Weights of 1.2 and 1.8 g are put on the different pixels of the multi-array. (b) The normalized resistance change versus pressure induced by bricks with the weight of 1.2 g and 1.8 g.
- Figure 2-28. The normalized resistance variations of the ITO crack sensor induced by fist movement.** (a) The ITO crack sensors are attached on the knuckles of the index and the middle fingers of a clenched fist. (b) The graphs represent the normalized resistance variations along with/according to the movements of the index (on the left) and middle (on the right) fingers when the hand is clenched into a fist. (c) When the hand opens, the curvature radius of the ITO crack sensor is diminished. (d) The graphs represent the ITO crack sensor normalized resistance variations due to the movements of the index (on the left) and the middle (on the right) fingers when the hand opens.
- Figure 3-1. Scotch tape test with an adhesion force of 4.5 N/25 mm for PI substrate crack sensor (reference number of 600, 3M).** (a) PI substrate crack sensor before scotch tape test. (b) Taped over the entire sensor. (c) After taking off the tape.
- Figure 3-2.** Experimental set up for measuring resistance variation.
- Figure 3-3. Schematic illustrations and SEM images of PI encapsulated crack sensor.** (a) The schematic illustration and optical microscope image of the PI encapsulated crack sensor. (b)

Scanning Electron Microscope (SEM) image of the crack sensor before encapsulation (left), and cross-sectional SEM image after encapsulation (right). (c) The schematic illustration of generated cracks on metal layer before stretching. (d) The schematic illustration of widened cracks after stretching.

- Figure 3-4.** **The performance comparison of the crack sensors in different environments.** (a) Performances of the sensors after thermal treatment, (b) Performances of the sensors after dipping in water, (c) Performances of the sensors dipping in saline solution (0.9 % NaCl).
- Figure 3-5.** The performance degradation by dipping into water: Red line is relative gauge factor degradation in 2 % strain, Blue line is that of 1 % strain.
- Figure 3-6.** Base line shift by dipping into water without straining.
- Figure 3-7.** **Delamination of metal film due to penetration of saline solution.** (a) PI encapsulated crack sensor before immersion. (b) PI encapsulated crack sensor after immersion in saline solution for 35 hours. (c) PDMS encapsulated crack sensor before immersion. (d) PDMS encapsulated crack sensor after immersion in saline solution for 15 hours.
- Figure 3-8.** **Comparison of performance changes according to PI encapsulation thickness.** (a) Resistance response in 2 % strain for various encapsulation thicknesses. (b) Gauge factor comparison by encapsulation thickness. (c) Performance comparison by encapsulation thickness in saline solution (0.9 % NaCl).
- Figure 3-9.** **Marathon test of the crack sensors up to 15000 cycles.** (a) Durability test result of the crack sensor on PET substrate. (b) Durability test result of the crack sensor on PI substrate. (c) Durability test result of the PI encapsulated crack sensor on PI substrate.
- Figure 3-10.** **The normalized resistance variations of the crack sensors with strain.** (a) The normalized resistance variance versus 2% strain in 10 times cyclic test of the crack sensor on PET substrate. (b) The crack sensor on PI substrate without the

encapsulating layer. (c) The crack sensor on PI substrate with the encapsulating layer. (d) Reproducible and hysteresis test obtained from crack sensors on PET substrate. (e) Crack sensors on PI substrate without the encapsulating layer. (f) The crack sensors on PI substrate with the encapsulating layer.

- Figure 3-11.** Strain-response curve of crack sensors.
- Figure 3-12.** The response time of the encapsulated crack based sensor.
- Figure 3-13.** **The schematic images of the FEP encapsulated crack sensor fabrication.** (a) The metal layer deposited PI film is impressed in between the double FEP films by 280°C, 50 bar in a second. (b) After impressing, cracks are formed by stretch the FEP films.
- Figure 3-14.** **The image of the FEP encapsulated crack sensor** (a) before water resist test, (b) after water resist test.
- Figure 3-15.** The graph of the FEP encapsulated crack sensor gauge factor varies with time in water.
- Figure 3-16.** The durability test of the FEP encapsulated crack sensors after the water resist test.
- Figure 3-17.** The durability comparison of the FEP encapsulated crack sensors (blue lines), and the PI encapsulated crack sensors (yellow lines).
- Figure 3-18.** **The photo images of the FEP encapsulated crack sensors after water resist test.** (a) No metal layers were peeled off from the PI substrate. (b) The metal layers on red dot area were peeled off from the PI substrate.
- Figure 3-19.** **The saline resist test of the FEP encapsulated crack sensors.** The encapsulated crack sensors withstand their performance until 15 days within saline conditions

Chapter 1. Introduction

1-1. Introduction

Improvement of technology to obtain health information for better, healthier life is in active progress [1-4]. This trend has led to increased demand for sensors that detect deformation or monitor human health and motions [5-6]. Recently, research on monitoring system has been focusing on the development of wearable and portable devices that detect human motions [5-9]. The wearable and portable system for monitoring human health needs to have properties of precision, lightness, flexibility, and attachability in order to adapt to human interfaces [10-16]. Also, to apply sensory devices on humans, transparency is required for aesthetic demand to adjust human face or skin [16, 17]. Diverse sensing mechanism for detecting fine deformation or monitoring human health has been widely studied in the research field [9, 18-24]. Some studies have presented sensing systems that make use of metal nanowire, carbon-nanotubes and grapheme combine with polymer substrates [9, 18-24]. These sensing systems are suitable to detect human motions or human health since they have flexibility and lightness to monitor the finger motion, pulse, vocal recognition, blood rate, facial expression, and temperature change.

Conventional strain gauges are widely used in industrial fields to measure

fine movements of turbine, car engines, and factory machines. However, since the conventional strain gauges have low sensitivity with the gauge factor ($GF = (R/R_0)/\epsilon$) of 2, these need data processing techniques to handle the data obtained from the strain gauges. Therefore, sensors with high sensitivity should replace the conventional sensory systems.

In 2014, strain and pressure detecting sensory system inspired by a spider's sensory system with mechanical crack has been reported [10]. The sensory system has nanoscale cracks on its a metal layer over a polymer substrate. Unlike convenient strain sensory systems, this sensory system uses electric resistance changes varied from cracks gap width with the applied strain. It has shown ultra-sensitivity to strain with the gauge factor over 2,000 and vibration measured up to 10 nm amplitude [10]. The mechanical crack sensory system is composed of a Pt metal layer as a conductive layer, and a substrate of a polyurethane acrylate (PUA) layer as a crack inducer on the Pt metal layer. Since the Pt metal layer cannot generate cracks below strain of 2%, PUA layer is used to induce the cracks on the Pt layer. However, the PUA substrate is not compatible to be directly deposited with other metals including gold (Au) and Silver (Ag) to generate defined cracks to sense motions due to poor adhesion between the PUA substrate and the metal film. Thus, to have diverse metallic film selection, improving the crack inducing layer is essential.

Recent research trends in health measurement devices are heading toward

continuously wearable health measurement. One of essential requirements for health measurement is transparency to secure convenience of use. Furthermore, transparent devices may extend to applications such as transparent display panels. Various research shows transparent sensory systems are based on carbon nanotubes, graphene, and metal nanowires. [16, 18, 22, 25-27] However, these sensory systems have limitations in terms of transparency or sensitivity [25–27]. To address this limitation, we present a transparent mechanical crack sensory system. The existing mechanical crack sensory system is opaque due to the Pt metal layer. Thus, we have replaced the Pt metal layer with a transparent conductive layer Indium Tin Oxide (ITO). The transparent crack sensors have high sensitivity to strain and high transparency up to 89% [28].

When sensory systems are applied to human interfaces or harsh environments, they may not be able to sustain their performance continuously due to damages from external conditions [10, 28-31]. To deal with this issue, we present stabilized crack-based sensory systems with encapsulations. In mechanical sensory systems, encapsulation is one of crucial issues to address for protection of the systems from external damages [32, 33]. With encapsulation, crack-based sensory systems can maintain their performance even in harsh conditions of water, chemical, or high temperature. Here, we present mechanical crack-based strain sensory systems with heat, water and saline solution resistance by alternating the substrate from polyester film to polyimide film and encapsulating the sensor with polyimide,

fluorinated ethylene propylene and oxide layers [34].

In *Chapter 2*, we propose diverse conductive materials layered crack-based sensory systems induced by a brittle thin layer [35]. Previous crack sensory systems have used a Pt metal layer as a conductive layer and a PUA layer as a crack inducing layer.[10] However, the PUA layer cannot induce cracks on Au and Ag metal layers. This poses huge restrictions in the choice of materials. Also, to form the PUA layer, at least 4 hours of UV curing is required. The curing process yields a disadvantage for mass production. In order to deal with this issue, inserting new inter layers could be a solution. Herein, we present an alternative mechanical crack sensory system with diverse materials (Au, Ag and Pt) by introducing a brittle metal Cr layer to generate cracks as defined to the other ductile metal layer with an oxide layer to enhance adhesion of the metal layer to the Polyethylene terephthalate (PET) film [36]. Our sensor has exhibited high sensitivity to strain (GF of Au and Ag metal layered crack sensors is about 1,700 at strain of 2% and that of a Pt metal layered crack sensor is about 900), reproducibility and durability. Furthermore, we present a transparent ITO crack sensory system [28]. An ITO layer has brittleness to generate cracks under the strain of 2%. Also, an ITO layer is a well-known transparent conductive material [36]. The transparent ITO crack sensory system is composed of an ITO layer as both conductive and crack induced layer and a PET

film as a substrate. This system has high transparency up to 89% and sensitivity to strain.

In *Chapter 3*, we present stabilized crack-based sensory systems with encapsulation [34]. To maintain the performance of sensory systems in a harsh environment, we encapsulate the crack sensors with the polymer and thin oxide layers. The encapsulated crack sensors maintain the performance under water, chemicals, and high temperature. The durability of crack-based sensors is dramatically increased with the encapsulation. The encapsulated crack sensors sustain the sensory performance up to 15,000 cyclic strain from 0% to 2%.

1-2. References

- [1] Honda, W., Harada, S., Arie, T., Akita, S., Takei, K., *Advanced Functional Materials* 2014, **24** (22), 3299-3304.
- [2] Gong, T., Zhang, H., Huang, W., Mao, L., Ke, Y., Gao, M., Yu, B., *Carbon* 2018, **140**, 286-295.
- [3] Jin, H., Abu-Raya, Y. S., Haick, H., *Adv Healthc Mater* 2017, **6** (11).
- [4] Choi, D. Y., Kim, M. H., Oh, Y. S., Jung, S. H., Jung, J. H., Sung, H. J., Lee, H. W., Lee, H. M., *ACS Appl Mater Interfaces* 2017, **9** (2), 1770-1780.
- [5] S. Lim, D. Son, J. Kim, Y. B. Lee, J.-K. Song, S. Choi, D. J. Lee, J. H. Kim, M. Lee, T. Hyeon, D.-H. Kim, *Adv. Funct. Mater.* 2015, **25**, 375.
- [6] M. Amjadi, A. Pichitpajongkit, S. Lee, S. Ryu, I. Park, *ACS nano* 2014, **8**, 5154.
- [7] S. Gong, W. Schwalb, Y. Wang, Y. Chen, Y. Tang, J. Si, B. Shirinzadeh, W. Cheng, *Nat. Commun.* 2014, **5**, 3132.
- [8] E. Roh, B.-U. Hwang, D. Kim, B.-Y. Kim, N.-E. Lee, *ACS nano* 2015, **9**, 6252.
- [9] S. Y. Hong, Y. H. Lee, H. Park, S. W. Jin, Y. R. Jeong, J. Yun, I. You, G. Zi, J. S. Ha, *Adv. Mater.*, 2016, **28**, 930.
- [10] D. Kang, P. V. Pikhitsa, Y. W. Choi, C. Lee, S. S. Shin, L. Piao, B. Park, K. Y. Suh, T. I. Kim, M. Choi, *Nature* 2014, **516**, 222.
- [11] S. Lee, A. Reuveny, J. Reeder, S. Lee, H. Jin, Q. Liu, T. Yokota, T. Sekitani,

- T. Isoyama, Y. Abe, Z. Suo, T. Someya, *Nat. Nanotechnol.* 2016, **11**, 472
- [12] D.-H. Kim, N. Lu, R. Ma, Y.-S. Kim, R.-H. Kim, S. Wang, J. Wu, S. M. Won, H. Tao, A. Islam, *science* 2011, **333**, 838.
- [13] G. Schwartz, B. C. Tee, J. Mei, A. L. Appleton, D. H. Kim, H. Wang, Z. Bao, *Nat Commun* 2013, **4**, 1859.
- [14] J. Lee, S. Kim, J. Lee, D. Yang, B. C. Park, S. Ryu, I. Park, *Nanoscale* 2014, **6** (20), 11932
- [15] S. Yang, Y. C. Chen, L. Nicolini, P. Pasupathy, J. Sacks, B. Su, R. Yang, D. Sanchez, Y. F. Chang, P. Wang, D. Schnyer, D. Neikirk, N. Lu, *Adv. Mater.* 2015, **27**, 6423.
- [16] B. U. Hwang, J. H. Lee, T. Q. Trung, E. Roh, D. I. Kim, S. W. Kim, N. E. Lee, *ACS Nano* 2015, **9**, 8801.
- [17] Lai, Y. C., Ye, B. W., Lu, C. F., Chen, C. T., Jao, M. H., Su, W. F., Hung, W. Y., Lin, T. Y., Chen, Y. F., *Advanced Functional Materials* 2016, **26** (8), 1286-1295.
- [18] S.-H. Bae, Y. Lee, B. K. Sharma, H.-J. Lee, J.-H. Kim, J.-H. Ahn, *Carbon* 2013, **51**, 236.
- [19] X. Li, R. Zhang, W. Yu, K. Wang, J. Wei, D. Wu, A. Cao, Z. Li, Y. Cheng, Q. Zheng, R. S. Ruoff, H. Zhu, *Sci. Rep.* 2012, **2**, 870.
- [20] J. Shi, Li, X. Li, H. Cheng, Z. Liu, L. Zhao, T. Yang, Z. Dai, Z. Cheng, E. Cheng, L. Yang, Z. Zhang, A. Cao, H. Zhu, Y. Fang, *Advanced Functional*

Materials 2016, **26** (13), 2078.

[21] X. Zhang, S. Hu, M. Wang, J. Yu, Q. Khan, J. Shang, L. Ba, *Nanotechnology* 2015, **26** (11), 115501.

[22] Z. Liu, D. Qi, P. Guo, Y. Liu, B. Zhu, H. Yang, Y. Liu, B. Li, C. Zhang, J. Yu, B. Liedberg, X. Chen, *Adv. Mater.* 2015, **27**, 6230.

[23] J. Zhang, J. Liu, R. Zhuang, E. Mader, G. Heinrich, S. Gao, *Adv Mater* 2011, **23** (30), 3392.

[24] K. K. Kim, S. Hong, H. M. Cho, J. Lee, Y. D. Suh, J. Ham, S. H. Ko, *Nano Lett* 2015, **15** (8), 5240

[25] D. J. Lipomi, M. Vosgueritchian, B. C. Tee, S. L. Hellstrom, J. A. Lee, C. H. Fox, Z. Bao, *Nat. Nanotechnol.* 2011, **6**, 788.

[26] Y.-C. Lai, B.-W. Ye, C.-F. Lu, C.-T. Chen, M.-H. Jao, W.-F. Su, W.-Y. Hung, T.-Y. Lin, Y.-F. Chen, *Adv. Funct. Mater.* 2016, **26**, 1286.

[27] T. Q. Trung, S. Ramasundaram, B. U. Hwang, N. E. Lee, *Adv. Mater.* 2016, **28**, 502.

[28] T. Lee, Y. W Choi, G. Lee, P. V. Pikhitsa, D. Kang, S. M. Kim, M. Choi, *J. Mater. Chem. C* 2016, **4** (42), 9947.

[29] Choi, Y.W., Kang, D., Pikhitsa, P.V., Lee, T., Kim, S.M., Lee, G., Tahk, D., Choi, M. *Scientific reports* **2017**, 7.

[30] Park, B., Kim, J., Kang, D., Jeong, C., Kim, K.S., Kim, J.U., Yoo, P.J., Kim, T.i. *Advanced Materials* **2016**, 28, 8130-8137.

- [31] WhanáChoi, Y., MoonáKim, S. *RSC Advances* **2017**, *7*, 34810-34815.
- [32] Viventi, J., Kim, D.-H., Vigeland, L., Frechette, E.S., Blanco, J.A., Kim, Y.-S., Avrin, A.E., Tiruvadi, V.R., Hwang, S.-W., Vanleer, A.C. *Nature neuroscience* **2011**, *14*, 1599-1605.
- [33] Viventi, J., Kim, D.-H., Moss, J.D., Kim, Y.-S., Blanco, J.A., Annetta, N., Hicks, A., Xiao, J., Huang, Y., Callans, D.J. *Science translational medicine* **2010**, *2*, 24ra22-24ra22.
- [34] Kim, T., Lee, T., Lee, G., Choi, Y., Kim, S., Kang, D., Choi, M., *Applied Sciences* 2018, **8** (3),
- [35] Lee, T., Choi, Y. W., Lee, G., Kim, S. M., Kang, D., Choi, M., *RSC Advances* 2017, **7** (55), 34810-34815.
- [36] T.-C. Li, C.-F. Han, K.-T. Chen, J.-F. Lin, *J. Display Technol.* 2013, **9**, 577.

Chapter 2. Brittle thin layer induced diverse conductive layer crack-based sensory systems

Published in Journal of Materials Chemistry C, 2016, 4, 9947-9953

Published in Journal of RSC Advances, 2017, 7, 34810-34815

2-1. Crack-based strain sensory system with diverse metal films by inserting brittle thin metal layer

2-1-1. Introduction

A sensing mechanism for human motions in the skin has been extensively studied in diverse engineering research fields. [1-6] Various sensory systems have been developed to have precision,[1, 7, 8] lightness,[3] flexibility,[2, 6, 9] and attachability to adapt to human's interfaces. [10, 11, 12] Dealing with these issues, some studies have presented sensory systems that make use of graphene,[13, 14, 15] carbon nanotubes,[16, 17, 18]and metal nanowire combined with polymer substrates. [19, 20] These sensing systems successfully detect human motions such as facial expression, finger motion, vocal recognition, pulse, blood rate, and temperature change. Of these, a mechanical crack sensory system has been recently

reported by using generated cracks on a polymeric substrate.[1, 7, 8, 21-23] The system showed high sensitivity defined by a linearly defined gauge factor (GF), with high durability and flexibility. The mechanical crack sensory system is composed with a Pt metal layer as a conductive layer, and a substrate of a polyurethane acrylate (PUA) layer which is used to induce cracks on the Pt metal layer. However, the PUA substrate is not compatible to be directly deposited with other metals including gold (Au) and silver (Ag) to generate defined cracks to sense motions, because of the low adhesion between the substrate and the metal film. [24, 25] This poses huge restrictions in the choice of materials. In the interaction of the metal layer and the polymeric layer for which adhesive force is an essential factor, compatibility is a very crucial issue in the field of sensory systems. In order to deal with this issue, inserting new inter layers could be a solution. Herein, we present an alternative mechanical crack sensory system with diverse materials (Au, Ag and Pt) by introducing a brittle metal Cr layer to generate cracks as defined to the other ductile metal layer with an oxide layer to enhance adhesion of the metal layer to the PET film. Our sensor has exhibited high sensitivity to strain (GF of Au and Ag metal layered crack sensors is about 1,700 at strain of 2% and that of a Pt metal layered crack sensor is about 900), reproducibility and durability.

2-1-2. Experimental

Metal layered crack sensors fabrication

5 nm of MoO₃ and 10 nm of Cr are deposited on the 30 μm Polyethylene terephthalate (PET) film by a thermal evaporator (Selcos Co., LTD.). On top of the Cr layer, 20 nm of Au or Ag is deposited by the thermal evaporator. Besides, Pt is deposited on the Cr layer by a sputter (Q300TD, Tescan Korea). For each metal layered crack sensor, cracks are generated on the sensors from stretching by a materials testing machine (3342 UTM, Instron Co.). Resistance is measured by a Lab View-based PXI-4071 system (National Instruments Inc.).

2-1-3. Results and Discussion

2-1-3-1. Composition of metal layered crack sensors

The schematic image in **Fig. 2-1a** shows the composition of the universal metal crack sensor. The crack sensor is composed of four layers, which are a conductive metal layer (Au, Ag, or Pt), an adhesion layer (Cr), a brittle oxide layer (MoO_3), and lastly substrate (PET) on the bottom. Thermal evaporator deposits a conductive metal layer (Au, Ag, or Pt), MoO_3 layer and Cr layer, of 30 nm, 5 nm and 10 nm, respectively, on a PET substrate film of 30 μm thickness. **Fig. 2-1b** is a photo image of the crack sensor devices including several kinds of metal layers on the top. For the conductive metal layer, Au, Ag, and Pt are used. These three metals have low electrical resistivity (Au: 22.14 $\text{n}\Omega\cdot\text{m}$, Ag: 16.87 $\text{n}\Omega\cdot\text{m}$, Pt: 105 $\text{n}\Omega\cdot\text{m}$ at 20 °C) and high ductility, so that these metal films typically do not make cracks on a PET substrate directly within strain of 2%. (**Fig. 2-2**)[24, 25] The key idea of the universal metal crack sensory system is to use a brittle layer as an interlayer to make stable cracks on a ductile metal layer so that we can detect the resistance change of the universally cracked conductive metal layer with the applied strain. (**Fig. 2-3**) The resistance change of the sensory system is characterized by the crack state. The resistance is increased as the opened cracks reduce the conductivity of the conductive metal layer while strain is applied on the sensors. In contrast, the resistance is decreased as the cracks are closed while the strain is released. **Fig. 2-2** shows the FESEM images of the conductive materials deposited on the PET

substrates without any interlayers. Although these substrates have been stretched with strain of 2%, the images show that no crack has been generated on the metal layers.

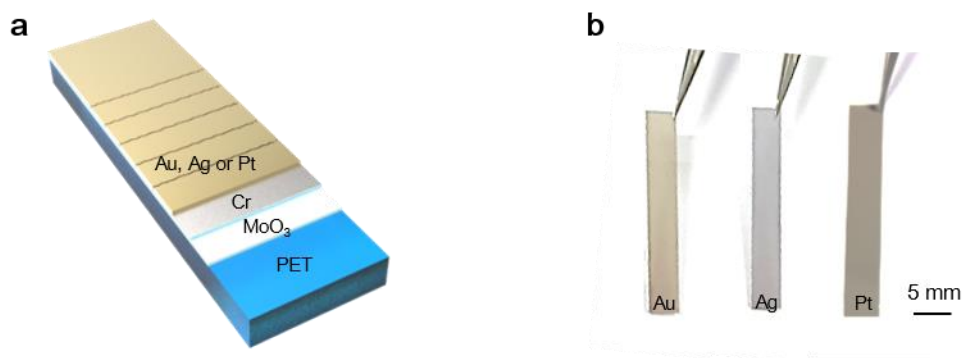


Figure 2-1. Schematic images of a metal layered crack sensor. (a) The image of a metal layered crack sensor with Cr and MoO₃ interlayers. (b) The real image of metal layered crack sensors. The sensors on the left side is an Au layered crack sensor. The sensors in the center are Ag layered crack sensors. The sensors on the right side are Pt layered crack sensors.

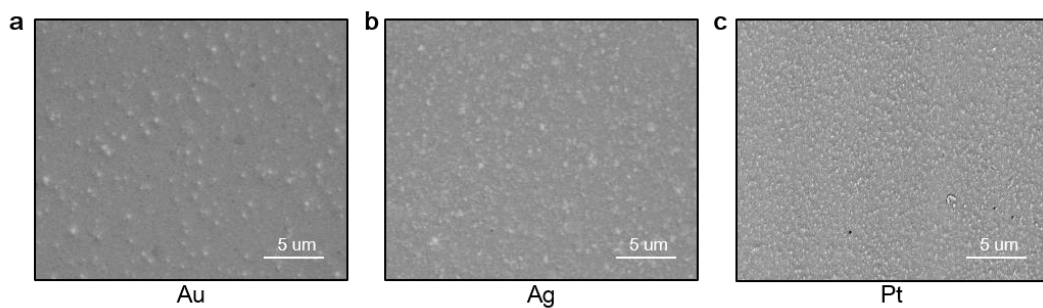


Figure 2-2. The SEM image of the conductive materials deposited on the PET substrates after applying strain of 2%. (a) Au deposited PET substrates after stretched strain of 2%. (b) Ag deposited PET substrates after stretched strain of 2%. (c) Pt deposited PET substrates after stretched strain of 2%.

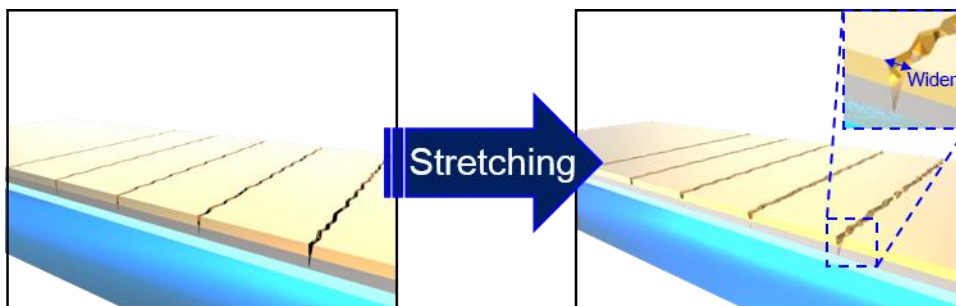


Figure 2-3. The illustration of the cracks on the sensor before stretching (left), and the cracks after stretching (right). The cracks on the conductive metal layer are induced by the cracks on the interlayer underneath the metal layer (the inserted image).

The SEM image in **Fig. 2-4a** shows the FESEM image of Cr/ MoO₃ layers deposited on the PET substrate after stretched with strain of 2%. This image presents that the cracks are well generated with regular intervals. When two layers are tightly bonded together, cracks on one side can be propagated to the other layer. Since the Cr layer is well known as an adhesion layer of Au, Ag and Pt layers,[24] the cracks initiated from the Cr layer are well propagated to the conductive material layer. **Fig. 2-4b, c, and d** show the FESEM image of the Au, Ag and Pt layered crack sensor with an interlayer (Cr and MoO₃). Interestingly, all of the conductive material layer crack sensors have the cracks with regular intervals similar with **Fig. 2-4a**. The average distance between the cracks of the Cr layer on PET substrate after stretching with strain of 2% is about 4.7 μm. Similarly, the average distance between the cracks of Au, Ag and Pt layered crack sensors are about 4.8 μm, 4.4 μm, and 5.0 μm, respectively. The cracks on the Cr layer and on the conductive material layer crack sensor display similarity in their distance from each other, because they propagate from the Cr layer onto the conductive layer.[24, 25] The Cr metal layer is not well attached on the PET substrate. To handle this problem, 5 nm of MoO₃ layer is deposited between PET substrates and the Cr layer. However, MoO₃ layer do not generate cracks with strain of 2%. (**Fig. 2-5**)

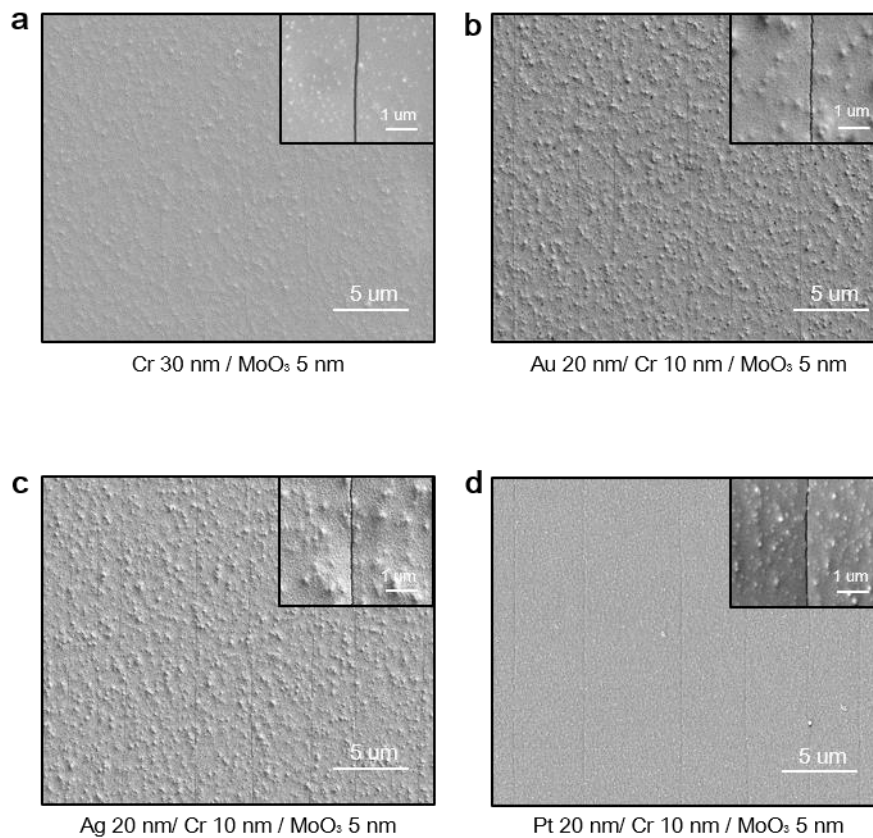


Figure 2-4. SEM images of the metal layered crack sensors. (a) The SEM image of Cr (30 nm) and MoO₃ (5 nm) on the PET substrate after strain of 2%. The inserted image is a magnified image of a crack on the Cr and MoO₃ layered PET substrate. (b) The SEM image of an Au layered crack sensor after strain of 2%. The inserted image is a magnified image of a crack on the Au layered crack sensor. (c) The SEM image of an Ag layered crack sensor after strain of 2%. The inserted image is a magnified image of a crack on the Ag layered crack sensor. (d) The SEM image of a Pt layered crack sensor after strain of 2%. The inserted image is a magnified image of a crack on the Pt layered crack sensor.

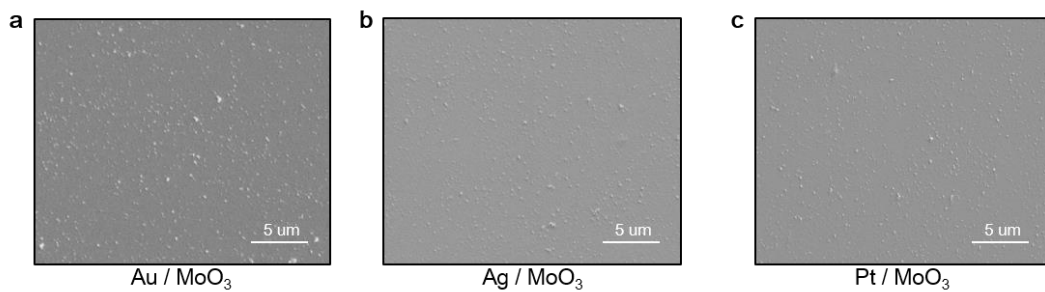


Figure 2-5. The SEM image of the conductive materials deposited on the MoO₃/PET substrates. (a) Au deposited MoO₃/PET substrates. (b) Ag deposited MoO₃/PET substrates. (c) Pt deposited MoO₃/PET substrates.

2-1-3-2. Measurements of the performance of the metal layered crack sensors

Fig. 2-6 shows the results of normalized resistance variation with strain for various metal layers. **Fig. 2-6a** is the graph of 10 cycles of the normalized resistance (R/R_0) variance of the Au layer crack sensor that varies from 0% to 2% of strain. The linearly defined gauge factor ($GF, (R/R_0)/\epsilon$) is over 1,700. **Fig. 2-6b** is the graph of 10 cycles of the normalized resistance variance of the Ag layer crack sensor that varies from 0% to 2% of strain. The GF is over 1,700. **Fig. 2-6c** is the graph of 10 cycles of the normalized resistance variance of the Pt layer crack sensor that varies from 0% to 2% of strain. The GF is over 900. We compare the conductive material layer crack sensors with the conductive material layer PET substrates without Cr and MoO_3 layers. **Fig. 2-7** is the graph of comparing the normalized resistance variances between the conductive material layer crack sensors and conductive material layer PET substrates without Cr and MoO_3 layers with strain from 0% to 2%. **Fig. 2-7a** is the graph of comparing the normalized resistance variances between an Au layer crack sensor (black line) and the Au layered PET substrate without Cr and MoO_3 layers (red line). Since the Au layer on the PET substrate is ductile, it does not generate cracks on the Au layer with strain from 0% to 2% (**Fig. 2-2a**). As a result, the Au layer on the PET substrate shows only slight normalized resistance change with strain from 0% to 2%. **Fig. 2-7b** is the graph of comparing the normalized resistance variances between an Ag layer crack sensor (black line)

and the Ag layered PET substrate without Cr and MoO₃ layers (blue line). **Fig. 2-7c** is the graph of comparing the normalized resistance variances between a Pt layer crack sensor (black line) and the Pt layered PET substrate without Cr and MoO₃ layers (green line). Like the Au layered PET substrate, Ag and Pt layered PET substrates without Cr and MoO₃ layers show only slight normalized resistance change with strain from 0% to 2%.

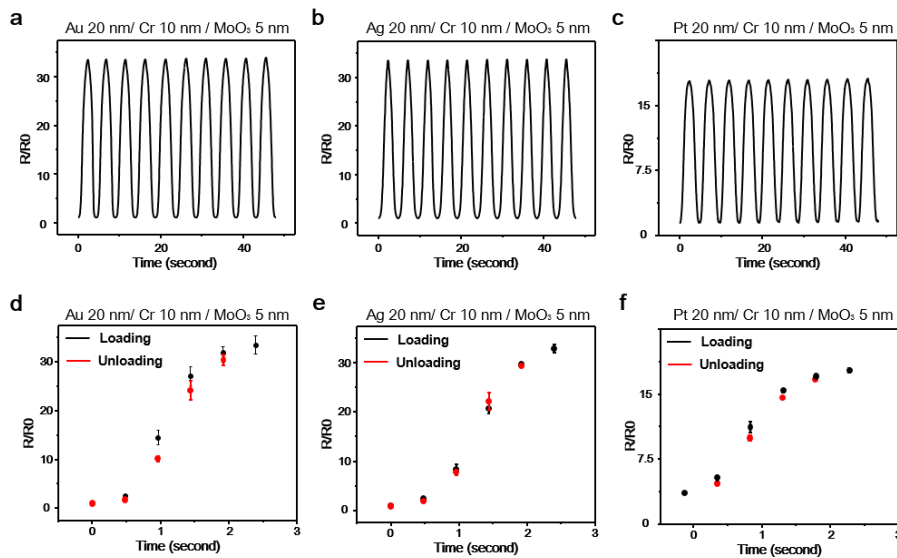


Fig. 2-6. The Performance graph of the metal layered crack sensors. (a) The graph of the Au layered crack sensors' normalized resistance variance versus strain of 2% in 10 cyclic tests. **(b)** The graph of the Ag layered crack sensors normalized resistance variance versus strain of 2% in 10 cyclic tests. **(c)** The graph of the Pt layered crack sensors normalized resistance variance versus strain of 2% in 10 cyclic tests. **(d)** The average and standard deviations of the 5 different Au layered crack sensors with hysteresis tests. Red dots show the unloading process and black dots show the loading process. **(e)** The average and standard deviations of the 5 different Ag layered crack sensors with hysteresis tests. Red dots show the unloading process and black dots show the loading process. **(f)** The average and standard deviations of the 5 different Pt layered crack sensors with hysteresis tests. Red dots show the unloading process and black dots show the loading process.

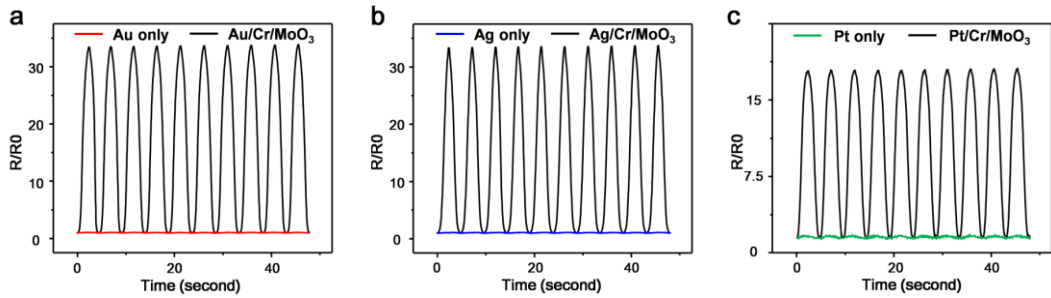


Figure 2-7. The graph of comparison between the conductive materials deposited on the PET substrates and the metal layered crack sensors with strain of 2% in a 10 time cyclic test. (a) The graph of comparison between the Au deposited on the PET substrates (red line) and the Au layered crack sensor (black line). (b) The graph of comparison between the Ag deposited on the PET substrates (blue line) and the Ag layered crack sensor (black line). (c) The graph of comparison between the Pt deposited on the PET substrates (blue line) and the Pt layered crack sensor (black line).

A previous study by Kang et al.¹ has fabricated the mechanical crack sensory system with Pt layer, PUA layer and a PET substrate. In this case, the PUA layer acts as the Cr layer of the conductive material layer crack sensors. **Fig. 2-8a** and **Fig. 2-8b** is the FESEM image of Au and Ag layer with the PUA layer and a PET substrate after stretching with strain of 2%. Both images show the Au and Ag layers with fine cracks on their surface that are generated by the PUA layers and transferred to them. However, even though the Au layer on the PUA layer has the cracks, it does not change the normalized resistance while it is stretched with strain of 2%. [26] **Fig. 2-9** is a comparative graph of the normalized resistance variance of the conductive material layer on the PUA layer and the conductive material layer crack sensors according to the strain of 2% in 10 cycles. **Fig. 2-9a** is the graph of comparing the normalized resistance variance between the Au layer crack sensor (black line) and the Au layer on the PUA layer (red line) with strain from 0% to 2%. The Au layer on the PUA layer shows negligible normalized resistance change compared to the resistance change of the Au layer crack sensor. **Fig. 2-9b** is the magnified graph of the normalized resistance change of the Au layer on the PUA layer with strain from 0% to 2%. **Fig. 2-9c** is the graph of comparing the normalized resistance variance between the Ag layer crack sensor (black line) and the Ag layer on the PUA layer (blue line) with strain from 0% to 2%. Likewise, the normalized resistance change with strain from 0% to 2% of Ag layer on the PUA layer is negligible. **Fig. 2-9d** is the magnified graph of the normalized resistance change of the Ag layer on the PUA

layer with strain from 0% to 2%. The reproducibility and hysteresis of conductive materials crack sensor are shown in **Fig. 2-6d, e and f**. **Fig. 2-6d** is the normalized resistance versus strain from 0% to 2% averaged over 5 different Au layer crack sensors along with error bars. Black dots represent the loading the sensors from 0% to the final strain of 2%, and red dots are for the unloading the sensors from 2% to the final strain of 0%. Likewise, **Fig. 2-6e and f** are graphs of the normalized resistance versus strain from 0% to 2% averaged over 5 different Ag and Pt layer crack sensors along with error bars. Black dots and red dots show normalized resistance when loading the sensors from 0% to 2%, and from 2% to 0%, respectively. Through **Fig. 2-6d, e and f**, the loading/unloading hysteresis of conductive material layer crack sensors is little. The small error bars in these figures show that the conductive material layer crack sensors have a high reproducibility. The reversible test of the conductive material layer crack sensors with variation strain of 0.5%, 1% and 2% are shown in the graph of **Fig. 2-10**. **Fig. 2-10a** is the reversible test of the Au layer crack sensor, **Fig. 2-10b** the test of the Ag layer crack sensor, and **Fig. 2-10c** the test of Pt layer crack sensor. The blue line is the strain from 0% to 2%, the red line is the strain from 0% to 2%, and the black line is the strain from 0% to 2%. The conductive material layer crack sensors show similar normalized resistance variance with strain from 0% to 0.5%, 1% and 2%. Another important performance is durability. We have performed 5,000 cyclic tests to conductive material layer crack sensors. **Fig. 2-11a, b and c** are the durability tests

of Au, Ag, and Pt layer crack sensors, respectively. However, conductive metal layer crack sensors without MoO₃ layer cannot maintain their performance in 5,000 cyclic test. (**Fig. 2-12**)

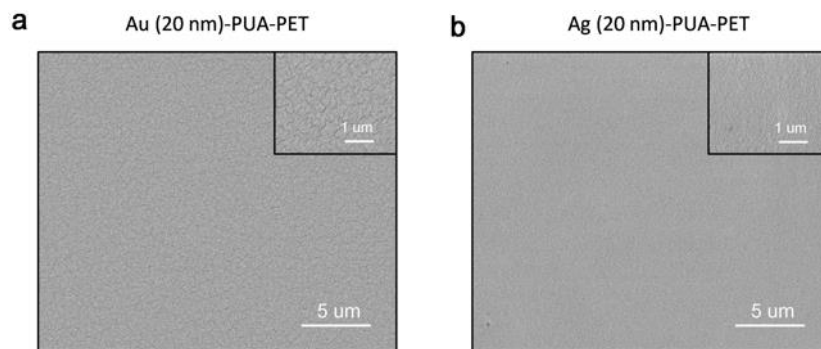


Figure 2-8. The SEM image of the conductive materials deposited on the PUA/PET substrates. (a) Au deposited PUA/PET substrates. (b) Ag deposited PUA/PET substrates.

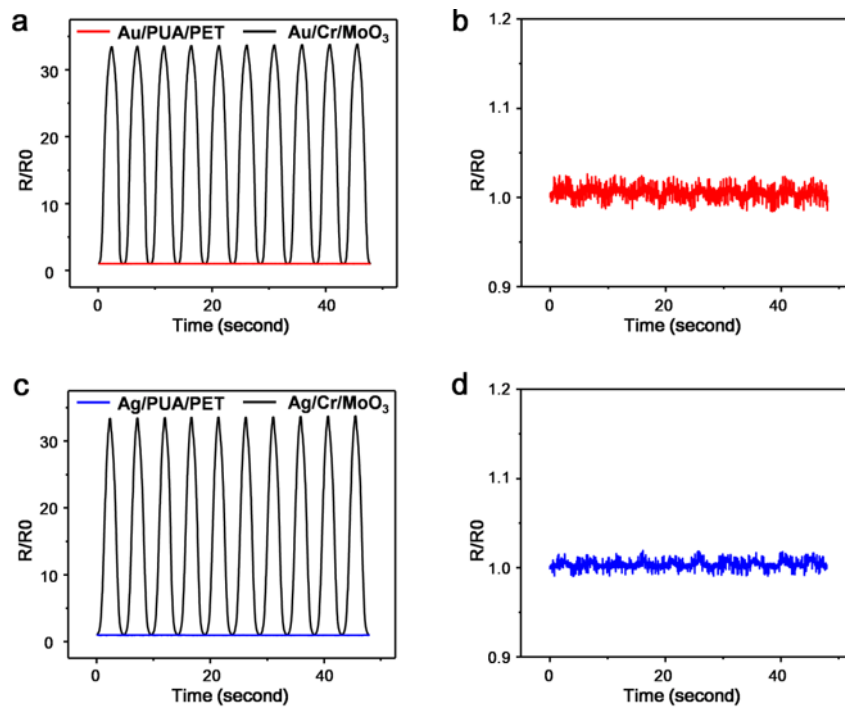


Figure 2-9. The graph of comparison between the conductive materials deposited on the PUA/PET substrates and the metal layered crack sensors with strain of 2% in a 10 time cyclic test. (a) The graph of comparison between the Au deposited on the PUA/PET substrates (red line) and the Au layered crack sensor (black line). (b) The Au deposited on the PUA/PET substrate graph of the normalized resistance variance versus strain of 2%. (c) The graph of comparison between the Ag deposited on the PUA/PET substrates (red line) and the Ag layered crack sensor (black line). (d) The Ag deposited on the PUA/PET substrate graph of the normalized resistance variance versus strain of 2%.

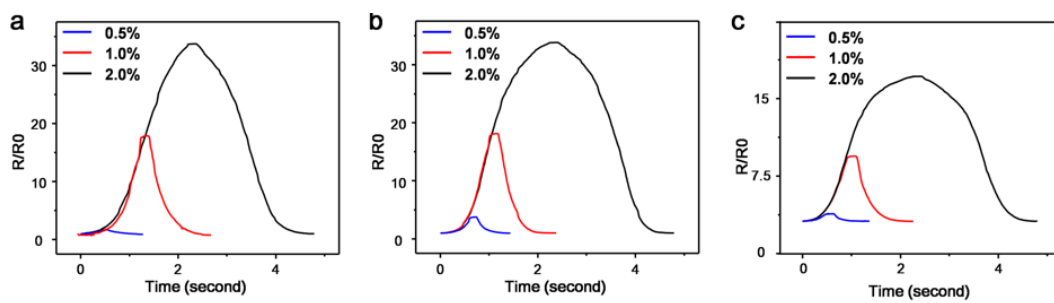


Figure 2-10. The graph for reversible tests with the metal layered crack sensors with various strains. The given strain on the sensor are 0.5% (blue line), 1.0% (red line), and 2.0% (black line). (a) The reversible test of Au layered crack sensor. (b) The reversible test of Ag layered crack sensor. (c) The reversible test of Pt layered crack sensor.

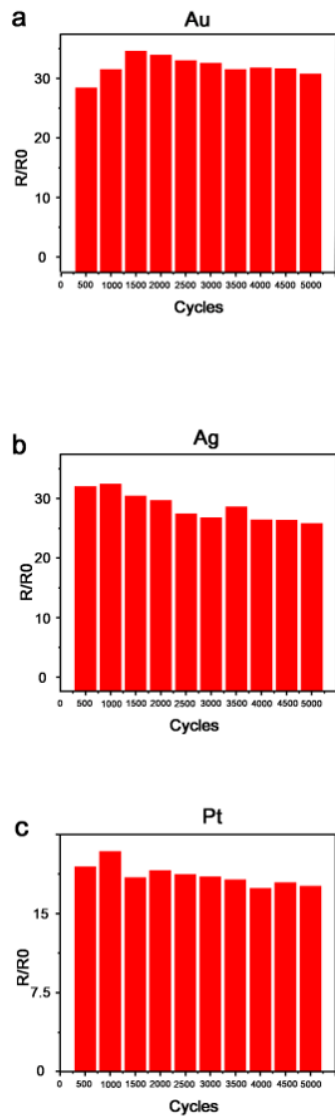


Figure 2-11. A marathon test of the conductive material layered sensors by repeating loading/unloading process about 5,000 cycles at strain from 0% to 2%. (a) A final normalized resistance of a marathon test at a certain period with an Au layered crack sensor, (b) an Ag layered crack sensor and (c) a Pt layered crack sensor

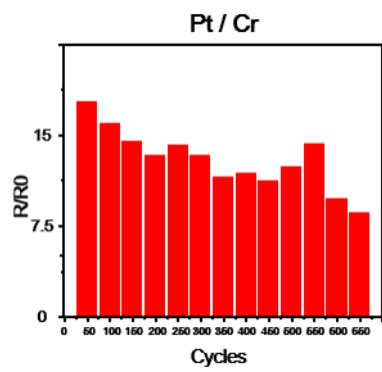


Figure 2-12. A marathon test of a Pt layered sensors without MoO₃ layer by repeating loading/unloading process about 650 cycles at strain from 0% to 2%.

2-1-3-3. Detecting the hands motion by using metal layered crack sensors

The conductive material layer crack sensors detect human motions. We apply the Au layer crack sensors on the human fingers. Since the sensor is made on the PET substrate, it has flexibility to mount on a human hand by sticking the ends of the sensor onto the knuckles of each finger. (**Fig. 2-13**) One of the experimenters put the two metal layered crack sensors on the knuckles of the index and ring fingers with the hand spread out as shown in **Fig. 2-13a**. Therefore, there is no resistance change of the crack sensors when the finger is spread. On the other hand, when the finger attached to the crack sensor is bent, the metal cracks on the sensor surface are opened and the resistance increases. In **Fig. 2-13**, we performed a rock-paper-scissors motion to verify that the crack sensors correctly indicate finger movements. **Fig. 2-13b** represents the clenching state of the hand, in which case the fingers are bent and the resistance of the crack sensor increases. In **Fig. 2-13b**, the hand is making a scissors motion for which the index finger is spread, while the ring finger is bent. Hence, there is resistance change in the Au layer crack sensor on the ring finger, while the crack sensor on the index finger shows no resistance change. In **Fig. 2-13c**, the hand is unfolded and there is no resistance change in the two Au layer crack sensors. The normalized resistance variances of the Au layer crack sensors with motion in the hand are shown in **Fig. 2-13d, e and f**. The red lines are the normalized resistance variance of the index finger, and the blue lines are the

normalized resistance variance of the ring finger. As shown in these figures, the normalized resistance increases when the finger is bent and the resistance decreases when the finger is spread.

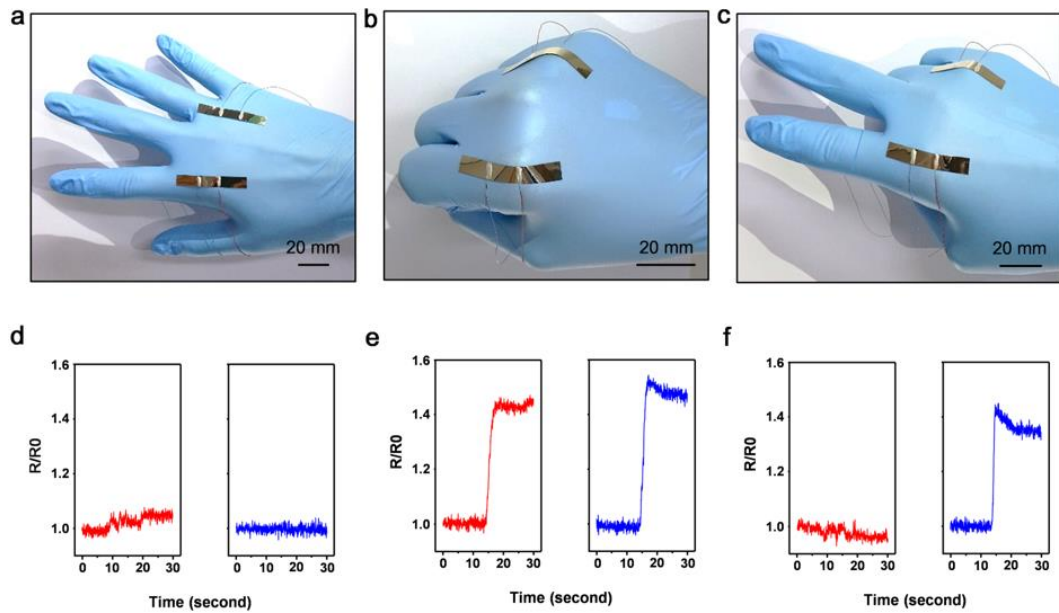


Fig. 2-13. Detecting the hands motion by Au metal layered crack sensors on the knuckles of the index and ring fingers (a) with the hand spread out, (b) with the hand clenched, (c) with the index finger spread out while the ring finger is clenched. (d) The graphs represent the Au metal layered crack sensors' normalized resistance variations due to the hand movement. The images on the left and right are the sensors on the index finger, and the ring finger, respectively, while (d) the hand spread out, (e) the hand clenched, and (f) the index finger spread out while the ring finger is clenched.

2-1-4. Summary

In conclusion, we report the Au, Ag and Pt layered crack sensor with inter-layers of Cr and MoO₃. Brittle metal Cr layer was used for generating cracks to other ductile metal layer while the MoO₃ layer was for enhancing adhesion between the PET film and the metal layers. Our sensor has exhibited high sensitivity to the applied strain (GF of Au and Ag metal layered crack sensors is about 1,600 at the strain of 2% and that of a Pt metal layered crack sensor is about 850). The reversibility, reproducibility, and durability of these metal layered crack sensors showed adaptability in human motion detection such as hand motion sensing. Our proposed method to construct crack sensor with the inter-layers can be one of the breakthroughs to overcome the compatibility issue for the crack sensor with low-adhesion substrate.

2-1-5. References

- [1] D. Kang, P. V. Pikhitsa, Y. W. Choi, C. Lee, S. S. Shin, L. Piao, B. Park, K. Y. Suh, T. I. Kim, M. Choi, *Nature* 2014, **516**, 222.
- [2] S. Lee, A. Reuveny, J. Reeder, S. Lee, H. Jin, Q. Liu, T. Yokota, T. Sekitani, T. Isoyama, Y. Abe, Z. Suo, T. Someya, *Nat. Nanotechnol.* 2016, **11**, 472
- [3] D.-H. Kim, N. Lu, R. Ma, Y.-S. Kim, R.-H. Kim, S. Wang, J. Wu, S. M. Won, H. Tao, A. Islam, *science* 2011, **333**, 838.
- [4] C. Pang, G. Y. Lee, T. I. Kim, S. M. Kim, H. N. Kim, S. H. Ahn, K. Y. Suh, *Nat Mater.* 2012, **11**, 795.
- [5] D. J. Lipomi, M. Vosgueritchian, B. C. Tee, S. L. Hellstrom, J. A. Lee, C. H. Fox, Z. Bao, *Nat. Nanotechnol.* 2011, **6**, 788.
- [6] G. Schwartz, B. C. Tee, J. Mei, A. L. Appleton, D. H. Kim, H. Wang, Z. Bao, *Nat Commun* 2013, **4**, 1859.
- [7] T. Lee, Y. W Choi, G. Lee, P. V. Pikhitsa, D. Kang, S. M. Kim, M. Choi, *J. Mater. Chem. C* 2016, **4 (42)**, 9947.
- [8] Y. W Choi, D. Kang, P. V. Pikhitsa, T. Lee, S. M. Kim, G. Lee, D. Tahk, M. Choi, *Sci Rep* 2017, **7**, 40116.
- [9] J. Lee, S. Kim, J. Lee, D. Yang, B. C. Park, S. Ryu, I. Park, *Nanoscale* 2014, **6 (20)**, 11932
- [10] S. Yang, Y. C. Chen, L. Nicolini, P. Pasupathy, J. Sacks, B. Su, R. Yang, D. Sanchez, Y. F. Chang, P. Wang, D. Schnyer, D. Neikirk, N. Lu, *Adv. Mater.* 2015,

27, 6423.

[11] B. U. Hwang, J. H. Lee, T. Q. Trung, E. Roh, D. I. Kim, S. W. Kim, N. E. Lee, *ACS Nano* 2015, **9**, 8801.

[12] E. Roh, B.-U. Hwang, D. Kim, B.-Y. Kim, N.-E. Lee, *ACS nano* 2015, **9**, 6252.

[13] S.-H. Bae, Y. Lee, B. K. Sharma, H.-J. Lee, J.-H. Kim, J.-H. Ahn, *Carbon* 2013, **51**, 236.

[14] X. Li, R. Zhang, W. Yu, K. Wang, J. Wei, D. Wu, A. Cao, Z. Li, Y. Cheng, Q. Zheng, R. S. Ruoff, H. Zhu, *Sci. Rep.* 2012, **2**, 870.

[15] J. Shi, Li, X. Li, H. Cheng, Z. Liu, L. Zhao, T. Yang, Z. Dai, Z. Cheng, E. Cheng, L. Yang, Z. Zhang, A. Cao, H. Zhu, Y. Fang, *Advanced Functional Materials* 2016, **26 (13)**, 2078.

[16] X. Zhang, S. Hu, M. Wang, J. Yu, Q. Khan, J. Shang, L. Ba, *Nanotechnology* 2015, **26 (11)**, 115501.

[17] Z. Liu, D. Qi, P. Guo, Y. Liu, B. Zhu, H. Yang, Y. Liu, B. Li, C. Zhang, J. Yu, B. Liedberg, X. Chen, *Adv. Mater.* 2015, **27**, 6230.

[18] J. Zhang, J. Liu, R. Zhuang, E. Mader, G. Heinrich, S. Gao, *Adv Mater* 2011, **23 (30)**, 3392.

[19] K. K. Kim, S. Hong, H. M. Cho, J. Lee, Y. D. Suh, J. Ham, S. H. Ko, *Nano Lett* 2015, **15 (8)**, 5240

[20] S. Gong, W. Schwalb, Y. Wang, Y. Chen, Y. Tang, J. Si, B. Shirinzadeh, W.

Cheng, *Nat. Commun.* 2014, **5**, 3132.

[21] H. Song, J. Zhang, D. Chen, K. Wang, S. Niu, Z. Han, L. Ren, *Nanoscale* 2017, **9** (3), 1166.

[22] T. Yang, X. Li, X. Jiang, S. Lin, J. Lao, J. Shi, Z. Zhen, Z. Li, H. Zhu, *Mater. Horiz.* 2016, **3** (3), 248.

[23] B. Park, J. Kim, D. Kang, C. Jeong, K. S. Kim, J. U. Kim, P. J. Yoo, T. I. Kim, *Adv Mater* 2016, **28** (37), 8130.

[24] B. Putz, R. L. Schoepner, O. Glushko, D. F. Bahr, M. J. Cordill, *Scr Mater* 2015, **102**, 23.

[25] Y. Xiang, T. Li, Z. Suo, J. J. Vlassak, *Applied Physics Letters* 2005, **87** (16), 161910.

[26] S. P. Lacour, S. Wagner, Z. Huang, Z. Suo, *Applied Physics Letters* 2003, **82** (15), 2404.

2-2. Crack-induced brittle transparent conductive materials sensory systems

2-2-1. Introduction

Recent research studies on transparent sensory systems is aim to adapt the systems into transparent display panel, or human's health care monitoring systems.[1-13] It is because the sensory systems with opaque surface have limitations on adaptability to display panels or human's interfaces.[1,14-16] Several transparent devices studies have been reported recently.[17-26] Among those, only a few researches are for strain sensory systems.[22-25] Although recent studied transparent sensory systems have high in transparency, these have relatively low sensitivity compare to the recent opaque strain sensory systems.[22-25] Thus, fabricating transparent strain sensory systems with high transparency and high sensitivity is still challenging. In 2014, Kang et al has shown the mechanical crack-based sensory systems with high sensitivity. [1] In *chapter 2-1*, we fabricated the crack sensory systems without polymer-based crack inducing layer. Rather than polymer-based crack inducing layer, we have used thin brittle metal layer, Cr. Cr layer is able to generate crack on the conductive metal epi-layer due to the brittleness and adhesive of Cr layer. However, the Cr induced crack sensors are composed of more than dual layer since Cr layer itself has poor conductivity. Considering this disadvantage, we have devised a transparent sensory system that

can be more simply fabricated. ITO layer is well known conductive materials.[18, 28, 29] It has high transparency and high conductivity. Also, ITO has brittleness to generate cracks below strain of 2%. Thus, ITO layer is adequate materials for transparent crack sensory systems. In this chapter, we have fabricated the transparent ITO crack-induced crack sensory system. It has high transparency with a clear view up to 89% (at wavelength of 560 nm), and high sensitivity to strain (GF of 4,000 at strain of 2%) and to pressure (sensitivity is about 1.91 kPa^{-1} at pressure of 30 – 70 kPa.). The sensory system consists of a ITO layer and a PET substrate only.

2-2-2. Experimental

Fabrication of transparent ITO crack sensory system:

The thickness of PET substrates is 30 μm . ITO is deposited on the PET substrates by a sputter. (sputter: Ultech Inc.) ITO deposition time is 45 minutes, with radio frequency (RF) power of 200 W. [18] We haven't done the post-annealing process. [30] The cracks on the crack sensors are formed by stretcher with materials testing machine (3342 UTM, Instron Co.). Lab View-based PXI 4071 system (National Instruments Inc.) measures the resistance change of the crack sensors.

2-2-3. Results and Discussion

2-2-3-1 mechanism of the transparent ITO crack sensory systems

The transparent ITO crack sensory systems has advantage in a simple fabrication. Simply, ITO is deposited on the PET substrate with the thickness of 600 nm. The thickness can be vary from 300 – 1000 nm. The thickness of the PET substrate is about 30 μm . After depositing ITO on the PET substrate, the cracks are generated on ITO layer with stretcher strain from 0% to 2% with 1,000 cycles. (**Fig. 2-14a**) After the 1,000 cycles with strain from 0% to 2%, the cracks are formed on the ITO layer. (**Fig. 2-14b**) As shown in **Fig. 2-14c**, the ITO crack sensors have clear view

even though the cracks are formed on the ITO layers. ITO layer is well known transparent electrode. Even though it has cracks on ITO crack sensors, the transparency is high where transmittance is 89% at the wavelength of 560 nm, and average transmittance is 79% at visible spectrum. (**Fig. 2-15**) In **Fig. 2-14b**, cracks are formed on the ITO layer. **Fig. 2-16** is magnified FESEM images of the crack on ITO layer after the cracks are formed. **Fig. 2-16a** is the image of the crack with strain of 0% and **Fig. 2-16b** is the image of the crack with strain of 2%. The yellow dot circles in **Fig. 2-16** indicates that the cracks on ITO layer are connected by small area. These explain the mechanism of continuous resistance changes while strain is held from 0% to 2%. We have tested the ITO crack sensor with various strains. As shown in **Fig. 2-17**, the data of 0.5% and 1.0% strain curve follow the 1.5% strain curve well. In **Fig. 2-17**, we have loading and unloading test then plot on the graph together. The hysteresis is small as shown in graph of **Fig. 2-17**. The ITO crack sensors show the resistance changes versus applied strain. **Fig. 2-18a** is the graph of ITO crack sensors resistance changes with applied strain from 0% to 2% in 10 cycles. **Fig. 2-18b** is the reproducibility testing graph. Average resistance changes up to 10 different samples of the ITO crack sensors are shown the dots on the graph of **Fig. 2-18b**. The bars on **Fig. 2-18b** is the standard derivations of resistance changes up to 10 different samples of the ITO crack sensors. **Fig. 2-19** is the graph for reversible tests of the ITO crack sensors with various strain ranges. The given strains on the sensor are 0.5%, 1.0% and 2%. The reversible test shows the ITO

crack sensors varies the resistance changes regardless of how much strains are applied. **Fig. 2-20** is the response time measurement of ITO crack sensors. The response time is about 1ms during the cycling with the stretch of 10 mm/min, which is acceptable for its applications. As seen in **Fig. 16**, the crack gap size is below 100 nm under strain of 2%. The crack gap sizes on the ITO crack sensors is much smaller than the wavelength of visible light. Thus, the ITO crack sensors have clear transparency without background image distortion. (**Fig. 2-21**). **Fig. 2-22** is the stress-strain curve of the ITO substrates with strain from 0% to 2%. The slope of the curve changes dramatically at strain of 2%. The sensitivity of the ITO crack sensors varies with the thickness of the ITO crack sensors. (**Fig. 2-23**)

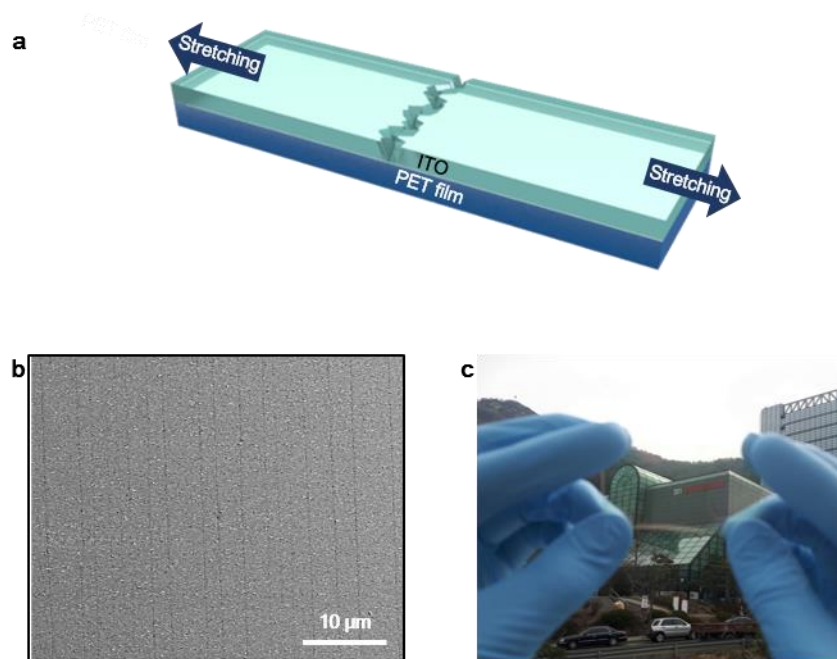


Figure 2-14. Schematic images of a transparent crack sensor. (a) The image of crack opening while cracks are generated with cyclic strain from 0% to 2%. (b) FESEM image in which the cracks on the sensor are parallel to each other. (c) The transparent ITO crack sensor shows clear view of background behind.

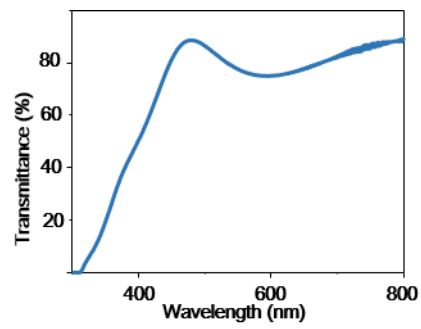


Figure 2-15. A graph of transmittance versus light wavelength through the crack sensor.

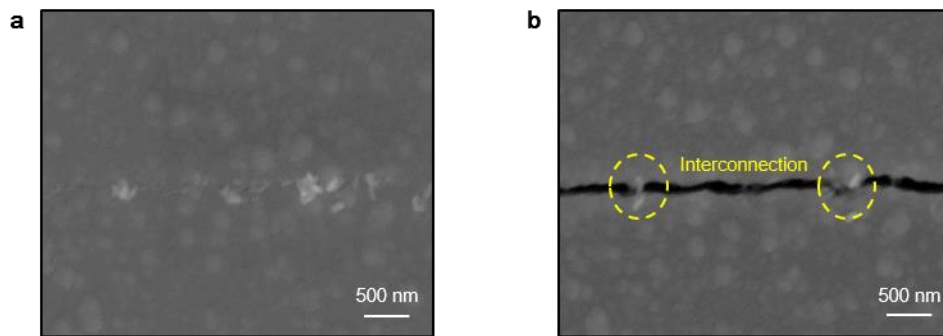


Figure 2-16. SEM images of crack opening. (a) SEM image of the crack on the ITO layer with no external tension. (b) SEM image of the crack on the ITO layer with strain of 2%.

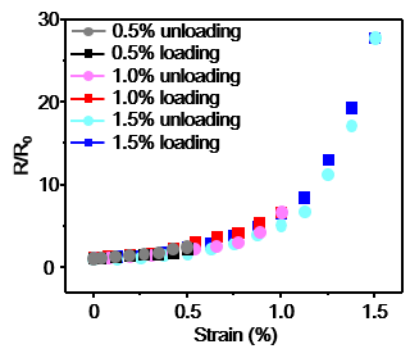


Fig. 2-17. The graph for loading/unloading tests with the ITO mechanical crack-based sensor with various strains.

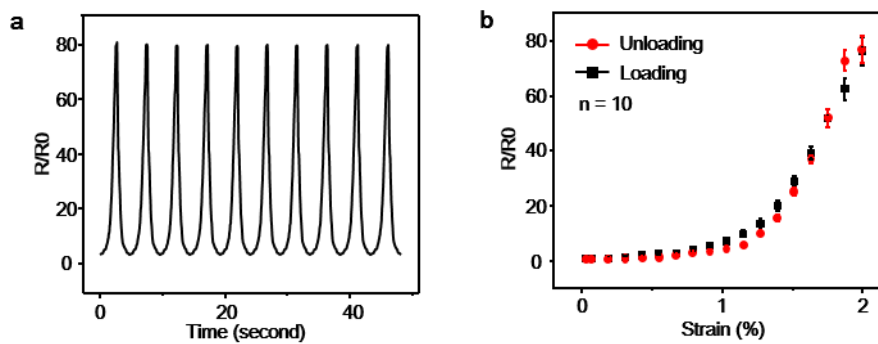


Figure 2-18. The variations of the performance of the ITO crack sensor with enhanced strain of 2%. (a) The graph of normalized resistance variance versus strain of 2% in a 10time cyclic test. **(b)** The standard deviation and the average over 10 different samples in the hysteresis test of the ITO crack sensor. Red and black dots show unloading and loading statuses, respectively.

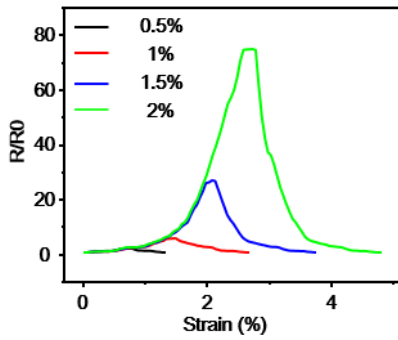


Figure 2-19. The graph for reversible tests with the ITO mechanical crack-based sensor with various strains. The given strains on the sensor are 0.5%, 1.0%, 1.5% and 2%.

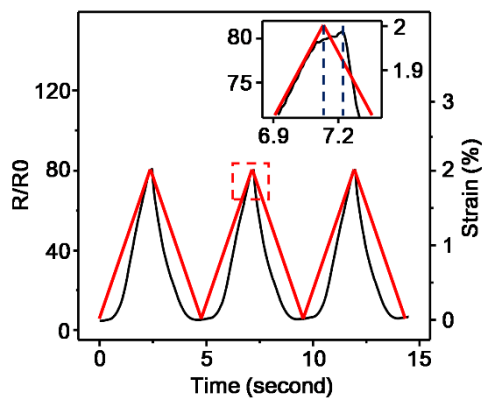


Figure 2-20. The graph of the ITO crack sensor response time.

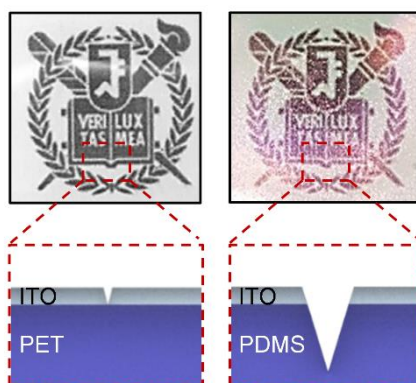


Figure 2-21. Images on the top show the ITO crack sensors on the PET film (on the left) and on the PDMS film (on the right) with their cross-sectional schematic illustrations below each image.

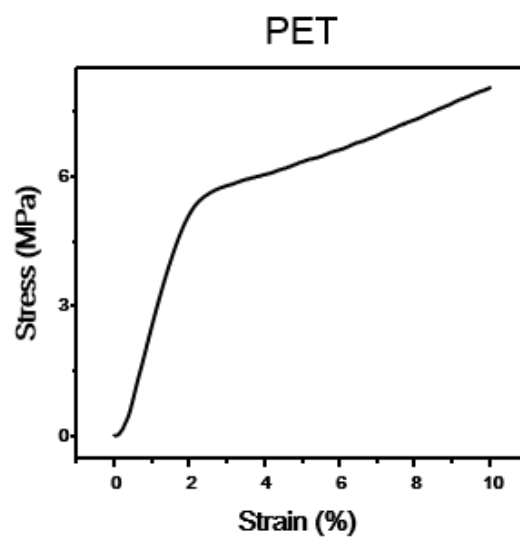


Figure 2-22. The graph of strain – stress curve of the PET substrate strain from 0% to 10%.

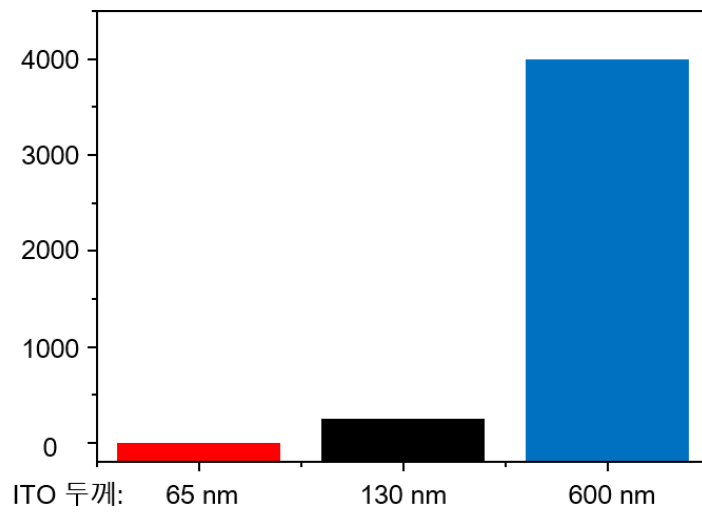


Figure 2-23. The gauge factor of the ITO crack sensors with different ITO thickness. (65 nm, 130 nm, 600 nm)

2-2-3-2 The pressure sensing with bended crack based sensors.

Every crack-based sensory systems have substrates which are stretched with tensile stress. In other words, the crack-based sensory systems can be used as pressure sensors when the substrates are bent by pressing the substrates on vertical direction of the pressure sensors. **Fig. 2-24** represents the schematic image of pressure sensing with the ITO crack film. In **Fig. 2-24a** shows how the pressure is applied on the crack sensors. The edges of the crack sensor are held onto two bars, and when pressure increases, the crack sensor is bent, cracks on the convex ITO surface are widen, and the cracks are opened. Thus, applied pressure is changing the resistance of crack-formed ITO layer. **Fig. 2-25** is the single unit pressure ITO sensor with an acrylic frame. The resistance varies while pressure is applied on the crack sensor. **Fig. 2-24b** is a graph of the normalized resistance versus pressure varying from 0 to 70 kPa. The slope of the curve of pressure versus normalized resistance at pressures from 0 to 30 kPa is about 0.21 kPa^{-1} and is about 1.91 kPa^{-1} in the range from 30 kPa to 70 kPa. We fabricated the ITO crack sensor with a sensing matrix of 4 by 4 pixels. Fabrication of multi-pixel ITO pressure sensors is on **Fig. 26**. Each of the ITO pressure sensing pixels has the area of 1 cm by 1 cm. Each pixel is held by PDMS pillars. Silver was used as a transparent electrode with the thickness of 13 nm. **Fig. 2-24** is an image of the ITO pressure sensor pixel matrix lying on a display panel of a mobile phone. The logo of SNU is clearly seen through the ITO pressure sensor. Plastic cylinders of 1.8 g and 1.2 g in weight were put and

pressed the ITO pressure sensor pixels. Resistance change of the pixels induced by the plastic weights is recorded and it shows that the sensor can measure both the position and the pressure at the same time (**Fig. 2-27b**).

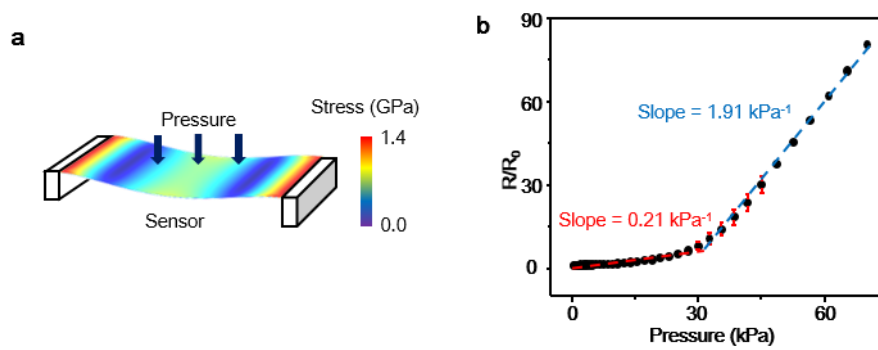


Figure 2-24. The transparent pressure sensor based on the ITO crack sensor mechanism. (a) The schematic image of the 4 by 4 ITO pressure sensor pixel matrix. The image on the bottom shows the visualized stress data of a single pixel of the pressure sensor. (b) The graph of normalized resistance versus pressure ranging from 0 to 70 kPa. The slope of the normalized resistance versus pressure from 0 to 30 kPa is 0.21 kPa^{-1} , and pressure from 30 to 70 kPa is 1.91 kPa^{-1} .

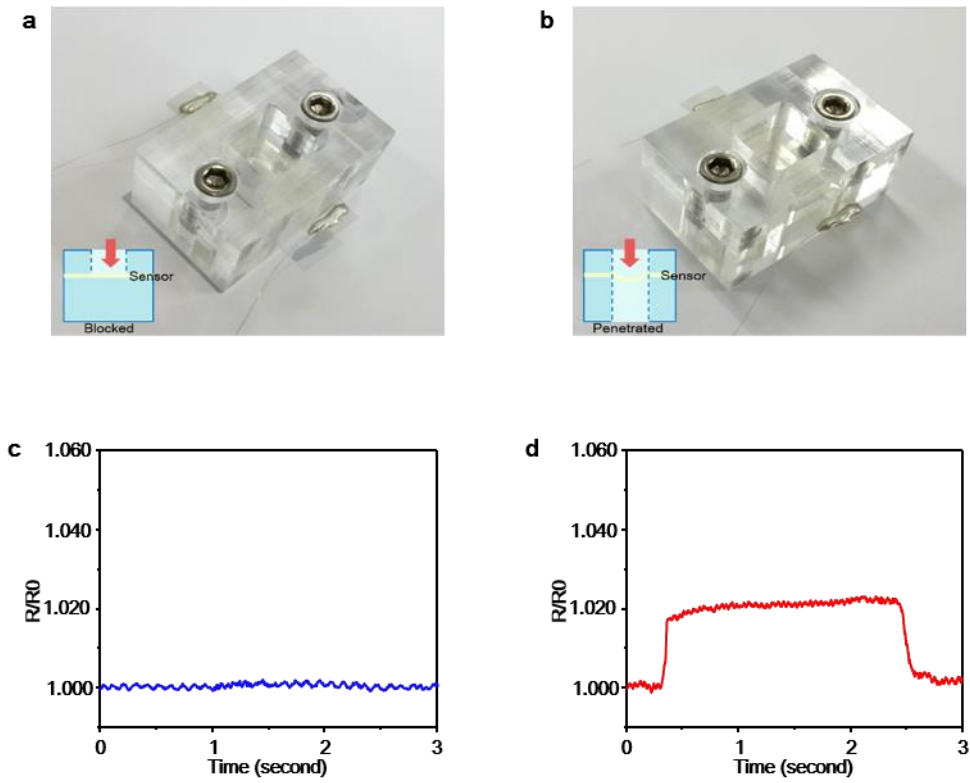


Figure 2-25. A single crack-sensor pressure detecting. (a) Photo image of acrylic frame for strain sensing mode. (b) Photo image of acrylic frame for pressure sensing mode. (c) Resistance change on the strain sensing mode with vertical pressure (0.15 kPa). (d) Resistance change on the pressure sensing mode with vertical pressure (0.15 kPa).

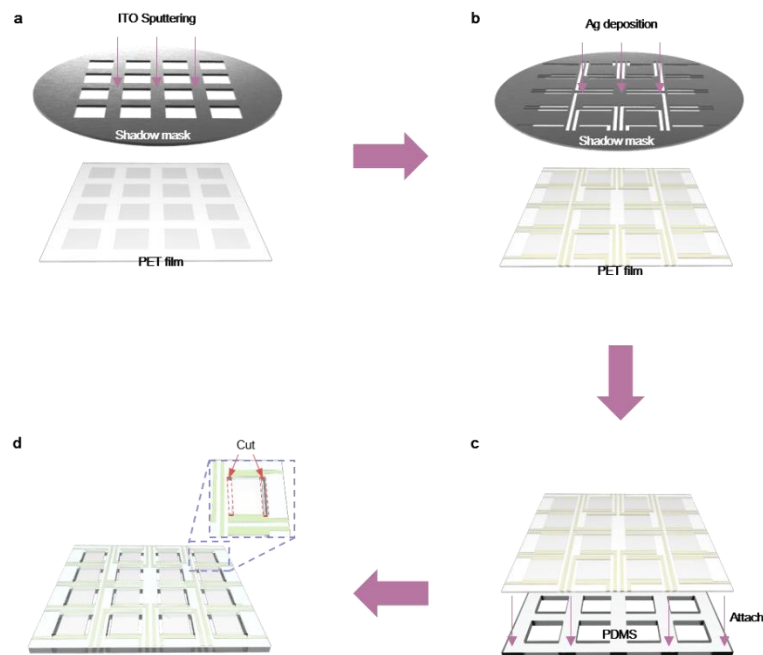


Fig. 2-26. Fabrication of the multi-pixel array pressure sensor. (a) ITO layer is deposited by a sputter on a PET substrate through a shadow mask. (b) Thin Ag metal layer (about 13 nm) is deposited on the ITO layer coated with the PET film by a thermal evaporator through an electrode path shadow mask. (c) A PDMS with 4 by 4 square hole is attached on the ITO layer coated with the PET film. (d) The edges of each pixel facing each other were cut.

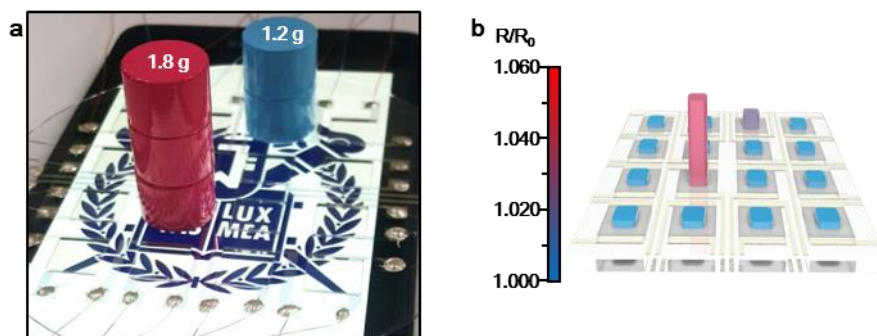


Figure 2-27. The multi-array based ITO pressure crack sensor (a) The photo image of the transparent pressure sensor multi-array on a display panel. Weights of 1.2 and 1.8 g are put on the different pixels of the multi-array. (b) The normalized resistance change versus pressure induced by bricks with the weight of 1.2 g and 1.8 g.

2-2-3-3 Hand motions sensing with bended crack based sensors.

The ITO crack sensor can detect motion in humans. Since it has sufficient flexibility, the sensor can easily be mounted on a human hand by attaching the ends of the sensor (see **Fig. 2-28a**) and measure the strain generated by the finger motion. To prove this, one of the experimenters has clenched human's fist and had two crack sensors mounted on his knuckles of the index and middle fingers as shown in **Fig. 2-28a**. As the radius of curvature of a knuckle is about 3 cm, the surface of the sensor is only slightly stretched as schematically shown in the inset image of **Fig. 2-28a** and it results in no resistance change (**Fig. 2-28b**). The human skin under the sensor can be seen and it demonstrates the transparency of the ITO crack sensor. The sensor on the knuckle is slightly folded when the hand opens as shown in **Fig. 2-28c** to make about 5 mm radius of curvature. The small curvature makes the surface of the sensor stretch and the sensor resistance is increased. The movement of each finger can be measured individually by the resistance change of each of the mounted sensors as shown in **Fig. 2-28d**.

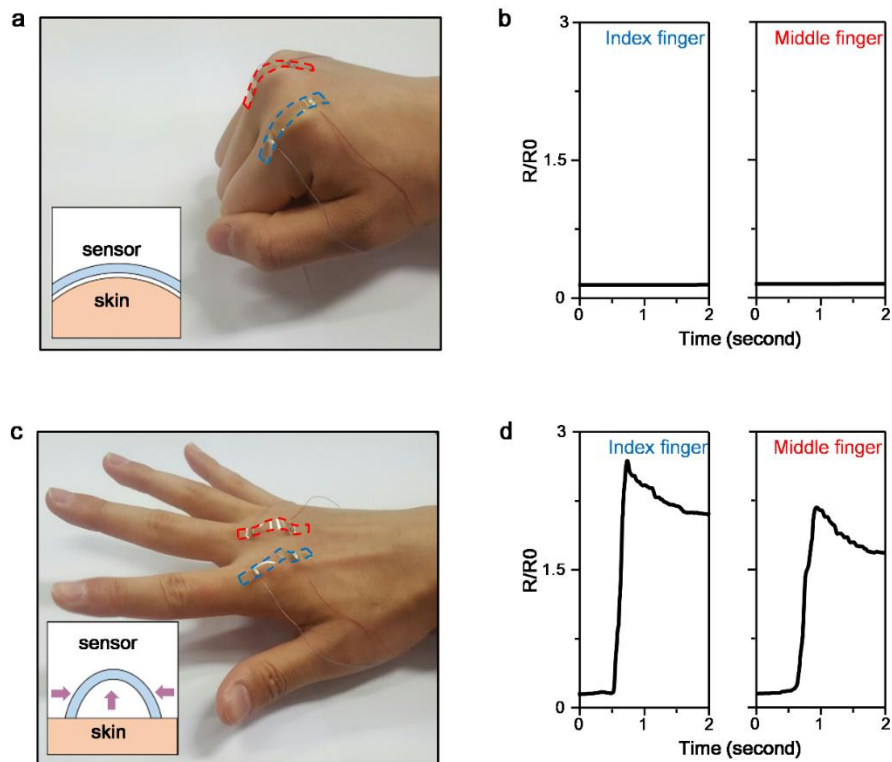


Figure 2-28. The normalized resistance variations of the ITO crack sensor induced by fist movement. (a) The ITO crack sensors are attached on the knuckles of the index and the middle fingers of a clenched fist. **(b)** The graphs represent the normalized resistance variations along with/according to the movements of the index (on the left) and middle (on the right) fingers when the hand is clenched into a fist. **(c)** When the hand opens, the curvature radius of the ITO crack sensor is diminished. **(d)** The graphs represent the ITO crack sensor normalized resistance variations due to the movements of the index (on the left) and the middle (on the right) fingers when the hand opens.

2-2-4. Summary

In summary, we report a transparent pressure and strain crack sensor with high sensitivity based on the parallel crack system on the ITO layer on a polymer substrate. It shows high gauge factors without losing transparency during stretching and can be applied as a multifunctional sensor for detecting strain, and pressure. The reproducibility, reversibility, flexibility, durability and large-area coverage through multiplexing enable the application of the device onto display panels.

2-2-5. References

- [1] D. Kang, P. V. Pikhitsa, Y. W. Choi, C. Lee, S. S. Shin, L. Piao, B. Park, K. Y. Suh, T. I. Kim, M. Choi, *Nature* 2014, **516**, 222.
- [2] D.-H. Kim, N. Lu, R. Ma, Y.-S. Kim, R.-H. Kim, S. Wang, J. Wu, S. M. Won, H. Tao, A. Islam, *science* 2011, **333**, 838.
- [3] S. Lee, A. Reuveny, J. Reeder, S. Lee, H. Jin, Q. Liu, T. Yokota, T. Sekitani, T. Isoyama, Y. Abe, Z. Suo, T. Someya, *Nat. Nanotechnol.* 2016.
- [4] S. Lim, D. Son, J. Kim, Y. B. Lee, J.-K. Song, S. Choi, D. J. Lee, J. H. Kim, M. Lee, T. Hyeon, D.-H. Kim, *Adv. Funct. Mater.* 2015, **25**, 375.
- [5] M. Amjadi, A. Pichitpajongkit, S. Lee, S. Ryu, I. Park, *ACS nano* 2014, **8**, 5154.
- [6] S. Yang, Y. C. Chen, L. Nicolini, P. Pasupathy, J. Sacks, B. Su, R. Yang, D. Sanchez, Y. F. Chang, P. Wang, D. Schnyer, D. Neikirk, N. Lu, *Adv. Mater.* 2015, **27**, 6423.
- [7] X. Wang, L. Dong, H. Zhang, R. Yu, C. Pan, Z. L. Wang, *Adv. Sci.* 2015, **2**,
- [8] C. M. Boutry, A. Nguyen, Q. O. Lawal, A. Chortos, S. Rondeau-Gagne, Z. Bao, *Adv. Mater.* 2015, **27**, 6954.
- [9] S. Gong, W. Schwalb, Y. Wang, Y. Chen, Y. Tang, J. Si, B. Shirinzadeh, W. Cheng, *Nat. Commun.* 2014, **5**, 3132.
- [10] E. Roh, B.-U. Hwang, D. Kim, B.-Y. Kim, N.-E. Lee, *ACS nano* 2015, **9**,

6252.

- [11] X. Li, R. Zhang, W. Yu, K. Wang, J. Wei, D. Wu, A. Cao, Z. Li, Y. Cheng, Q. Zheng, R. S. Ruoff, H. Zhu, *Sci. Rep.* 2012, **2**, 870.
- [12] S. Choi, H. Lee, R. Ghaffari, T. Hyeon, D. H. Kim, *Adv. Mater.* 2016.
- [13] S. Y. Hong, Y. H. Lee, H. Park, S. W. Jin, Y. R. Jeong, J. Yun, I. You, G. Zi, J. S. Ha, *Adv. Mater.*, 2016, **28**, 930.
- [14] J. Park, M. Kim, Y. Lee, H. S. Lee, H. Ko, *Sci. Adv.* 2015, **30**
- [15] K. K. Kim, S. Hong, H. M. Cho, J. Lee, Y. D. Suh, J. Ham, S. H. Ko, *Nano Lett.* 2015, **15**, 5240.
- [16] Z. Wang, S. Wang, J. Zeng, X. Ren, A. J. Chee, B. Y. Yiu, W. C. Chung, Y. Yang, A. C. Yu, R. C. Roberts, A. C. Tsang, K. W. Chow, P. K. Chan, *Small* 2016.
- [17] Q. Sun, H. Kim do, S. S. Park, N. Y. Lee, Y. Zhang, J. H. Lee, K. Cho, J. H. Cho, *Adv. Mater.* 2014, **26**, 4735.
- [18] T.-C. Li, C.-F. Han, K.-T. Chen, J.-F. Lin, *J. Display Technol.* 2013, **9**, 577.
- [19] P. Gutruf, C. M. Shah, S. Walia, H. Nili, A. S. Zoolfakar, C. Karnutsch, K. Kalantar-zadeh, S. Sriram, M. Bhaskaran, *NPG Asia Mater.* 2013, **5**, e62.
- [20] M. Ramuz, B. C. Tee, J. B. Tok, Z. Bao, *Adv. Mater.* 2012, **24**, 3223.
- [21] X. Zhang, S. Hu, M. Wang, J. Yu, Q. Khan, J. Shang, L. Ba, *Nanotechnology* 2015, **26**, 115501.
- [22] D. J. Lipomi, M. Vosgueritchian, B. C. Tee, S. L. Hellstrom, J. A. Lee, C. H. Fox, Z. Bao, *Nat. Nanotechnol.* 2011, **6**, 788.

- [23] B. U. Hwang, J. H. Lee, T. Q. Trung, E. Roh, D. I. Kim, S. W. Kim, N. E. Lee, *ACS Nano* 2015, **9**, 8801.
- [24] Y.-C. Lai, B.-W. Ye, C.-F. Lu, C.-T. Chen, M.-H. Jao, W.-F. Su, W.-Y. Hung, T.-Y. Lin, Y.-F. Chen, *Adv. Funct. Mater.* 2016, **26**, 1286.
- [25] S.-H. Bae, Y. Lee, B. K. Sharma, H.-J. Lee, J.-H. Kim, J.-H. Ahn, *Carbon* 2013, **51**, 236.
- [26] T. Q. Trung, S. Ramasundaram, B. U. Hwang, N. E. Lee, *Adv. Mater.* 2016, **28**, 502.
- [27] Z. Liu, D. Qi, P. Guo, Y. Liu, B. Zhu, H. Yang, Y. Liu, B. Li, C. Zhang, J. Yu, B. Liedberg, X. Chen, *Adv. Mater.* 2015, **27**, 6230.
- [28] J. Park, D. Tahk, C. Ahn, S. G. Im, S.-J. Choi, K.-Y. Suh, S. Jeon, *J. Mater. Chem.* 2014, **2**, 2316.
- [29] B. J. Kim, D. H. Kim, Y.-Y. Lee, H.-W. Shin, G. S. Han, J. S. Hong, K. Mahmood, T. K. Ahn, Y.-C. Joo, K. S. Hong, N.-G. Park, S. Lee, H. S. Jung, *Energy Environ. Sci.* 2015, **8**, 916.
- [30] H. Morikawa, M. Fujita, *Thin Solid Films* 2000, **359**, 61.

Chapter 3. Stabilized crack-based sensory systems with encapsulation

Published in Applied Sciences, 2018, 8(3), 367

3-1. Crack sensors encapsulation.

3-1-1. Introduction

Sensor encapsulation is a crucial issue that needs to be taken care of in order to increase its applicability to various research fields. For example, bio-implantable devices, artificial skin, and wearable sensors need to endure wet and biochemical environments and encapsulation of the device would guarantee the device performance [1 - 12]. Recently, a new type of mechanosensor inspired by a spider's sensory organ system has been reported, which includes nanoscale cracks on metallic layer over a polymer substrate [13]. This spider-inspired sensor dramatically changes its electric resistance with the applied strain which widens the crack width. It also shows incredibly high sensitivity to strain with its extremely high gauge factor, over 2000 and vibration which is estimated to be measurable up to 10 nm amplitude [13]. The gauge factor GF, one of the most important indicator of the sensitivity of strain sensors, is defined as $GF = (\Delta R/R_0)/\epsilon$. Where ΔR is the resistance change with deformation, R_0 is the resistance before deformation, and ϵ is the applied deformation. Moreover, it has diverse advantages including flexibility, wearability, and multifunctional sensing abilities [13 - 17]. However, the durability of the sensor in harsh environments of liquids and/or high temperature, is still a

challenging issue. Sensor systems are usually exposed to various surrounding environments including different surrounding liquid, humidity and temperature, which lead to the damage the sensory system and shortening of the sensor's life. To solve this matter, we have demonstrated the extended capability of the crack sensory system by replacing the substrate from polyethylene terephthalate (PET) to Polyimide (PI) and encapsulating the sensor with PI. Because the polyimide is widely used in flexible electronics or sensor systems due to its high durability and flexibility [2 – 18, 19]. Also, Fluorinated ethylene propylene (FEP) is used to encapsulate the crack sensors. There are various advantages in applying our crack based sensor system. Furthermore, Jonathan Viventi et al. has developed a device encapsulated with polyimide, demonstrating new opportunities for the sensors to be applied in clinical fields [20, 21]. The encapsulated crack sensor can be used in diverse industries such as a wearable voice/pulse/motion sensor, strain gauge sensor at high temperature, vibration monitoring sensor for identifying internal damage to bridges, ultra-sensitive pressure/force sensor for surgical devices, and skin attachable health monitoring sensor.

3-1-2. Experimental

The fabrication of an encapsulated thin metal layered crack sensor

The basic features of the encapsulated crack sensor are demonstrated in Figure 1a. The sensor was 5 mm in width and 50mm in length, and the gauge length was 30 mm. It was composed of five layers: 7.5 μm thick PI film (3022-5 Kapton thin film, Chemplex) or 6 μm thick PET film (3026 Mylar thin film, Chemplex) as the bottom substrate layer, 5 nm thick molybdenum trioxide (MoO_3) as an adhesion layer, 50 nm thick chromium (Cr) as a crack inducing layer, 30 nm thick gold (Au) for an electrical conductor, and lastly 650 nm thick cured polyimide film (Poly (pyromellitic dianhydride-co-4,4'-oxydianiline), amic acid solution, Sigma-Aldrich) on the top layer for the encapsulation of the total system. The PI precursor was spin-coated on the cracked metal films and it was cured on a hot plate in the N_2 atmosphere (80 $^\circ\text{C}$ for 30 min and 290 $^\circ\text{C}$ for 30 min). MoO_3 is known as an adhesion layer between metal and polymer [17], and we simply tested it with “scotch tape test” [22]. It was confirmed that no defect occurred when the scotch tape was attached and detached on the metal surface. (**Fig. 3-1**) The thin film layers (MoO_3 , Cr, and Au) on the polymer substrate are deposited by the thermal evaporation system (Thermal Evaporation System, DD high tech Co.). The thickness of deposited metals and polymers are measured by AFM measurement. FEP film (Teflon TM) is prepared to encapsulate the crack sensors. Thickness of FEP films are 25 μm and 50 μm . The crack sensor is inserted between two FEP films and heat is applied to attach the FEP films on the sensor. Before attachment, drill two holes on the one of the FEP films which wire can pass through. The FEP films are heated with temperature of 280 $^\circ\text{C}$ at pressure of 50 bar for a second. After

the heating, wires are bonded on the crack sensor through the holes on the FEP films.

Thermal, Water, and Saline solution resistance test

To verify the performance of the device to detect vibration and strain in harsh environments such as liquid environment or a steam turbine blade, we tested the sensors in three different conditions (at high temperature, in water, and in saline solution). And in these conditions, we also compared the sensors with three different types of substrates: sensors with a PET substrate without encapsulation, a PI substrate without encapsulation, and an encapsulated PI substrate. Each sensor was heated on a hot plate for 10 minutes at 100 °C, 200 °C and 300 °C and checked for each gauge factor by 50 cycles of straining from 0 to 2 %. For water and saline solution resistance tests, the sensors were dipped into water or saline solution for a certain period of time (1, 10, 30 hours for water resistance test and 12, 24, 36 hours for saline solution resistance test) and checked for the gauge factor by 50 cycles of straining from 0 to 2 % after being dried out in the ambient condition.

Measuring resistance variation

Fig. 3-2 shows the experimental set up for measuring resistance variation by straining of sensor. The sensors were stretched from 0 to 2 % strains up to 15000 times repeatedly with the sweeping speed of 20 mm/min to measure the durability by using a material testing machine (3342 UTM, Instron Co.). The variation of resistance of the metal layered crack sensors was measured simultaneously by Lab View-based data acquisition system (PXI-4071, National Instruments Inc.). Standard deviation of the measurement when measuring 2 wire resistance with 5 1/2 digit was 0.01 Ω .

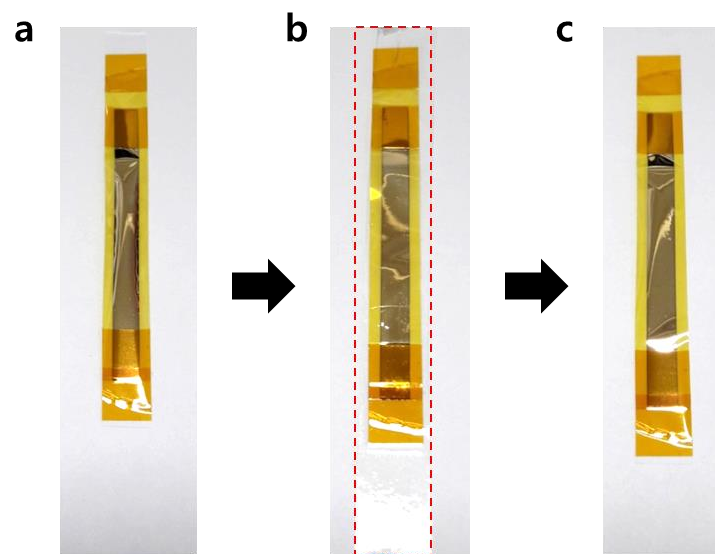


Figure 3-1. Scotch tape test with an adhesion force of 4.5 N/25 mm for PI substrate crack sensor (reference number of 600, 3M). (a) PI substrate crack sensor before scotch tape test. (b) Taped over the entire sensor. (c) After taking off the tape.

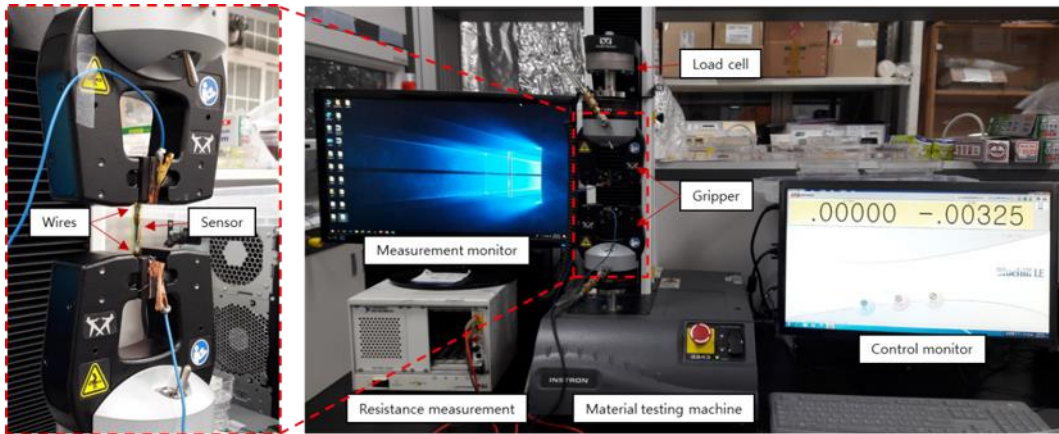


Figure 3-2. Experimental set up for measuring resistance variation.

3-1-3. Results and Discussion

3-1-3-1. Polyimide Encapsulated crack sensors

In general, metal layers on the crack lips can be delaminated by repetitive stretching, heating, and in water or chemical environments [23 – 32]. From Repeated exposure to these environments, a sensor can have stress concentration on the edge due to different Poisson's ratio or thermal expansion mismatch [23, 25, 33]. A water or chemical environment causes degradation of the adhesion force between the metal film and the polymer substrate [32]. To measure the durability of our crack sensors; we have performed three kinds of experimental tests: Thermal resistance test, water & saline solution resistance test, and marathon test.

In order to protect the crack sensor from the harsh environment and improve the durability, we encapsulated crack based sensor with PI. The schematic illustration of PI encapsulated crack based sensor is presented in **Fig. 3-3a**. The crack on the thin films was generated by stretching them at 2% strain before encapsulation (**Fig. 3-3b left**). And the polyimide precursor solution was spin-coated on the thin cracked metal film. The cross-sectional SEM image (**Fig. 3-3b right**) shows that the solution does not penetrate into the gap of a crack because the gap was too narrow (10~15 nm). **Fig. 3-3c** illustrates the cracks generated in the transverse direction to the extension force, and the crack gap increases with applied strain as shown in **Fig. 3-3d**. The gauge factor of the encapsulated sensor reached above 10,000 at a strain of 2% with high reproducibility and durability.

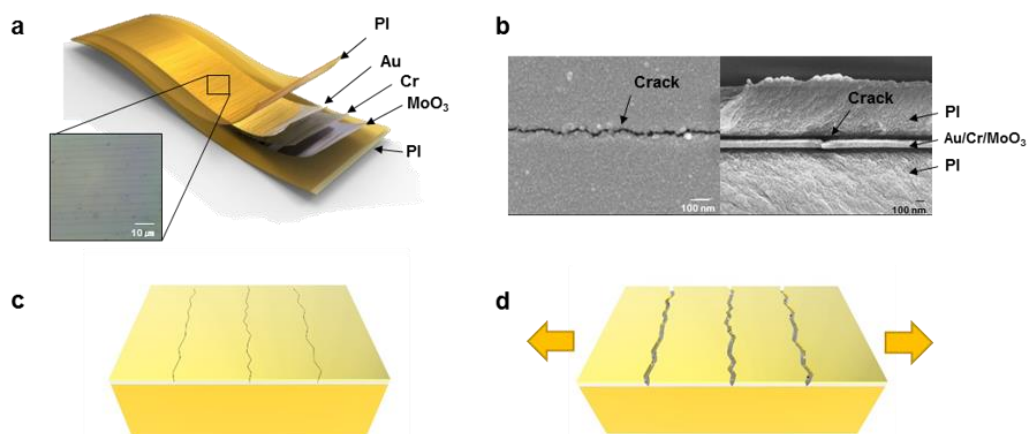


Figure 3-3. Schematic illustrations and SEM images of PI encapsulated crack sensor. (a) The schematic illustration and optical microscope image of the PI encapsulated crack sensor. **(b)** Scanning Electron Microscope (SEM) image of the crack sensor before encapsulation (left), and cross-sectional SEM image after encapsulation (right). **(c)** The schematic illustration of generated cracks on metal layer before stretching. **(d)** The schematic illustration of widened cracks after stretching.

The results in **Fig. 3-4** represent that the thermal, water and saline solution durability of the crack sensor have been greatly improved with encapsulation by cured PI. In the thermal resistance test (**Fig. 3-4a**), the PET substrate of the crack sensor maintained its gauge factor for about 90 % at 200 °C because the deformation of polymer surface reduced the stress concentration at the metal-polymer interface by going above glass-transition temperature($T_g = 85 \text{ }^\circ\text{C}$) [34]. However, it starts to break down when it is heated up to 300 °C, exceeding the melting temperature of the PET ($T_m = 290 \text{ }^\circ\text{C}$) [35]. And In the case of the PI substrate crack sensor without encapsulation, the relative GF rapidly decreased by heating, although the PI substrate was supposed to endure at the temperature above 300 °C. This was due to the delamination caused by different thermal expansion coefficient and weak adhesive force between the metal layer and the polymer substrate [36]. However, for the encapsulated crack sensor, the gauge factor remained as 77 % even after heating at 300 °C. The top encapsulating layer was responsible for enduring the heat treatment, which prevents the delamination of the metal layer from the substrate.

The graphs in **Fig. 3-4b** clearly show that sensors without encapsulation are very vulnerable in liquid environment. The metal layer of the PET substrate crack sensor delaminated as soon as it is immersed in water and the PI substrate crack sensor cannot resist either liquid. However, the PI encapsulated crack sensor could endure 30 hours in water and 24 hours in 0.9 % saline water with the gauge factor of 2 % strain even though the relative gauge factor decreased to 50 %. But we could see that straining 2 % in a state where the adhesion force was degraded due to wet conditions accelerated degradation of its gauge factor. **Fig. 3-5** shows that when the strain range was from 0% to 1%, the sensor maintains its GF 90% or more for 130 hours, and **Fig. 3-6** shows that there was no base resistance change for 190 hours

without straining. Because the actual operating range of the sensor would not be higher than 1%, it could endure longer in a wet environment.

Fig. 3-4c, PI is also verified as a very good passivation layer compared with PDMS by its water permeability. Compared to a sensor encapsulated with a PDMS of 30 μm thickness, it showed superior performance in saline solution. The major cause of GF decreases in liquid environment is delamination. In **Fig. 3-7**, the PI or PDMS encapsulated crack sensor immersed in saline solution shows that the metal layer is separated from the substrate, which indicates an increase of the base line. But the delamination issue in these environments can be enhanced by thicker encapsulation layer. In **Fig. 3-8** shows that if the thickness of the encapsulation layer is increased to 10 μm , it can last more than 100 hours in saline solution, but it must be appropriately adjusted because it is in a trade-off relationship with the sensitivity of the sensor (**Fig. 3-8a and b**). These results show a large expandability of the crack sensor in a humid environment, such as a wearable device.

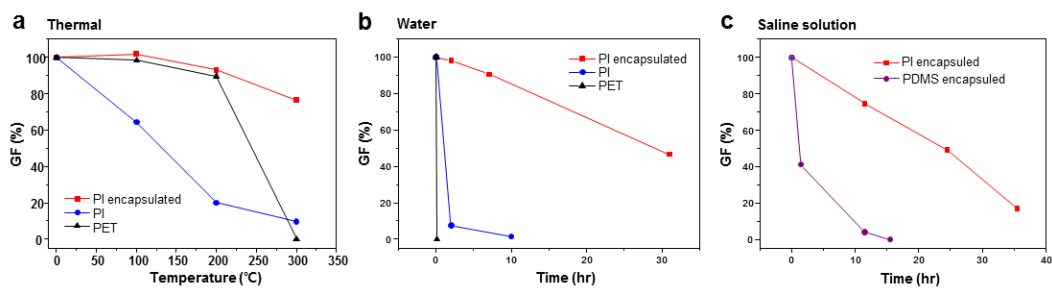


Figure 3-4. The performance comparison of the crack sensors in different environments. (a) Performances of the sensors after thermal treatment, **(b)** Performances of the sensors after dipping in water, **(c)** Performances of the sensors dipping in saline solution (0.9 % NaCl).

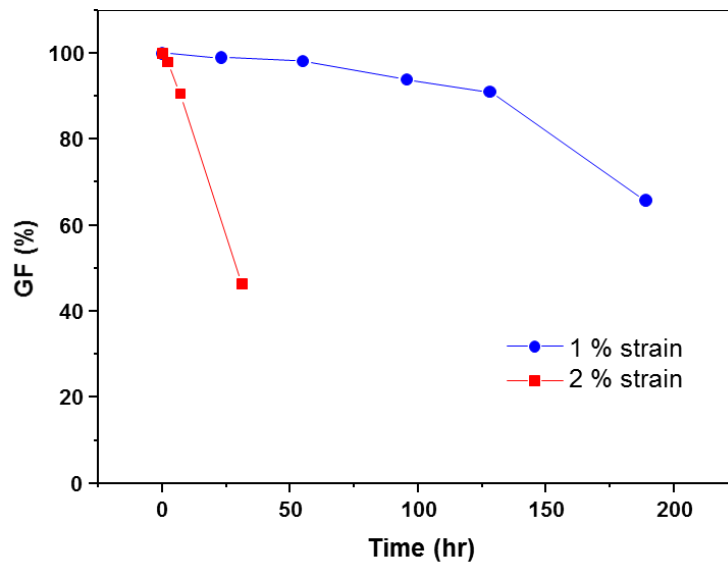


Figure 3-5. The performance degradation by dipping into water: Red line is relative gauge factor degradation in 2 % strain, Blue line is that of 1 % strain.

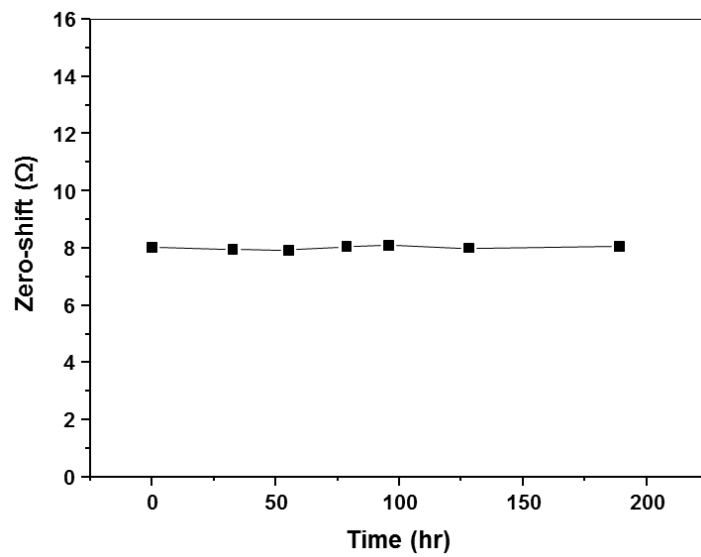


Figure 3-6. Base line shift by dipping into water without straining.

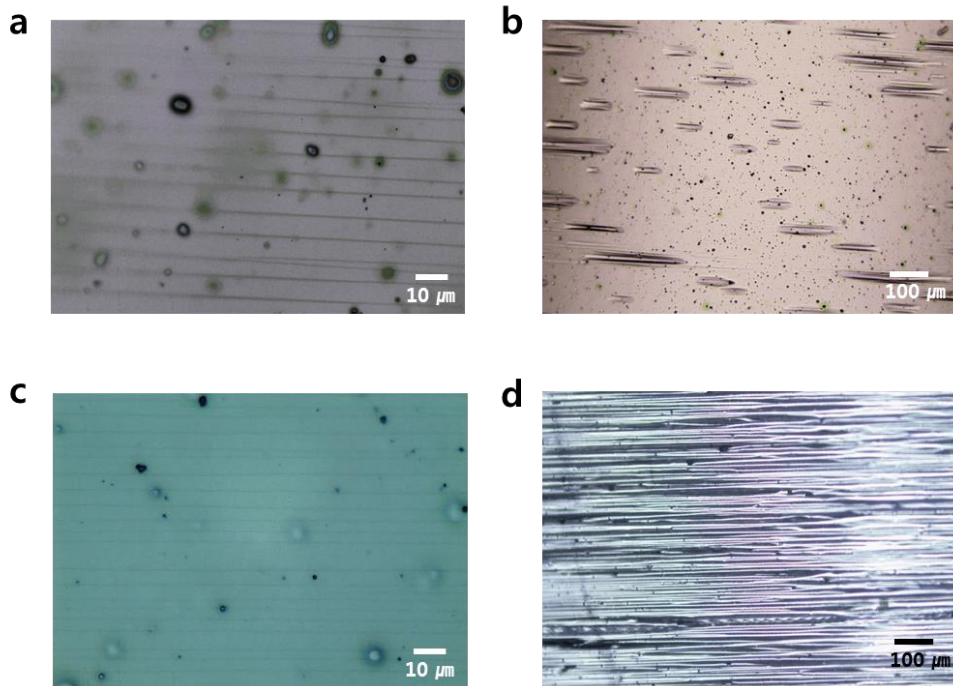


Figure 3-7. Delamination of metal film due to penetration of saline solution.

(a) PI encapsulated crack sensor before immersion. (b) PI encapsulated crack sensor after immersion in saline solution for 35 hours. (c) PDMS encapsulated crack sensor before immersion. (d) PDMS encapsulated crack sensor after immersion in saline solution for 15 hours.

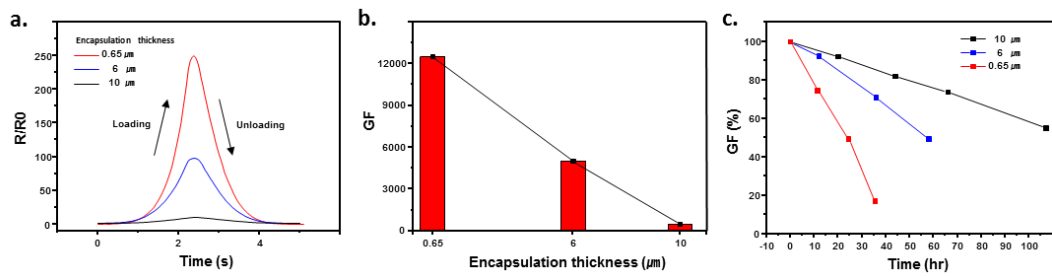


Figure 3-8. Comparison of performance changes according to PI encapsulation thickness. (a) Resistance response in 2 % strain for various encapsulation thicknesses. **(b)** Gauge factor comparison by encapsulation thickness. **(c)** Performance comparison by encapsulation thickness in saline solution (0.9 % NaCl).

Fig. 3-9 shows durability (marathon test) performance of the sensors up to 15000 cycles. First, the crack sensor on PET substrate without the encapsulating layer lose its gauge factor rapidly by 20 % from the first 1000 to 15000 cycles of repetitive stretching (**Fig. 3-9a**). Second, the GF of the crack sensor on PI substrate without the encapsulating layer increased until 3000 cycles and started to decrease gradually until 7000 cycles, and it became 30 % of maximum GF at 15000 cycles (**Fig. 3-9b**). The reason why the sensitivity increased first then decrease was that deepening of crack depth by penetration and incomplete recovery of crack gap by residual stress occurred simultaneously. When crack penetrates into the substrate, sensitivity increases by deepening the crack depth [16]. But repetitive straining accumulates residual stress on the crack vertex, disturbing closing of the crack gap, the gauge factor decreases [37]. Third, the crack sensor on PI substrate with the encapsulating layer had lower sensitivity than that of the crack sensor on PI substrate without encapsulation, but sensitivity drop with repeated tensile load improved slightly. It maintains its GF upper than 65 % until 11000 cycles (**Fig. 3-9c**). These results show that the encapsulating layer contributes to delay of the progress of the crack.

The resistance of the metal films on the polymer substrate dramatically increases due to the crack gap opening by stretching it up to 2%. To use it as a sensor, the reverse process should return the initial crack gap and its initial resistance as well. **Fig. 3-10a, b, and c** show that 10-cycle set of strains from 0 % to 2 % at a sweeping speed of 20 mm/min with 1 second of the interval was nearly identical. The linearly fitted gauge factor of crack sensor on PET substrate with the strain range from 0 % to 2 % by regression analysis was ~2800, that of the crack sensor on PI substrate was 28000 and that of the PI encapsulated crack sensor was 12500. Interestingly, it shows that only by changing substrates from PET to PI, sensitivity increased up to 10 times. We assume that this phenomenon was caused

by crack penetration into the PI substrate because the sensitivity of the sensor increases as the depth of crack increases [16]. **Fig. 3-11** shows that the change in resistance of three samples when applied strain from 0 % to 2 %. The result exhibits the change in resistance to the applied strain of the PI encapsulated crack sensor was more linear than the other sensors. However, the PI encapsulation process induces reduced gauge factor about ~45 %. **Fig. 3-10d, e, and f** each shows a graph of the averaged normalized resistance of three different samples along with an error bar. (n=5) Black square marks are for the loading to the strain of 2 %, and red circle marks are for unloading. The response time of the sensor was about 5 ms (**Fig. 3-12**). It shows that these three different types of sensors had quite good reproducibility without hysteresis.

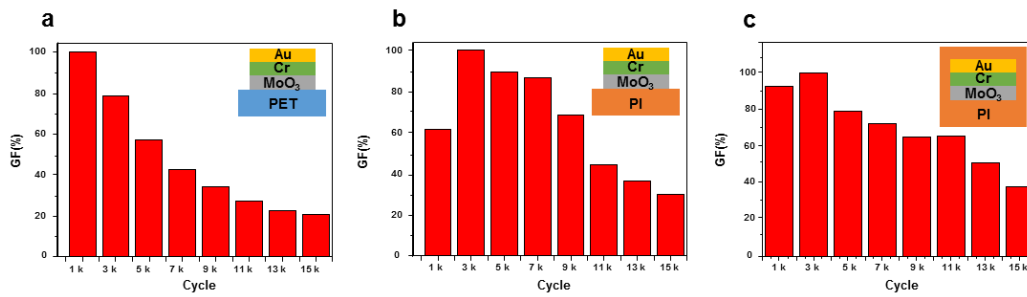


Figure 3-9. Marathon test of the crack sensors up to 15000 cycles. (a) Durability test result of the crack sensor on PET substrate. (b) Durability test result of the crack sensor on PI substrate. (c) Durability test result of the PI encapsulated crack sensor on PI substrate.

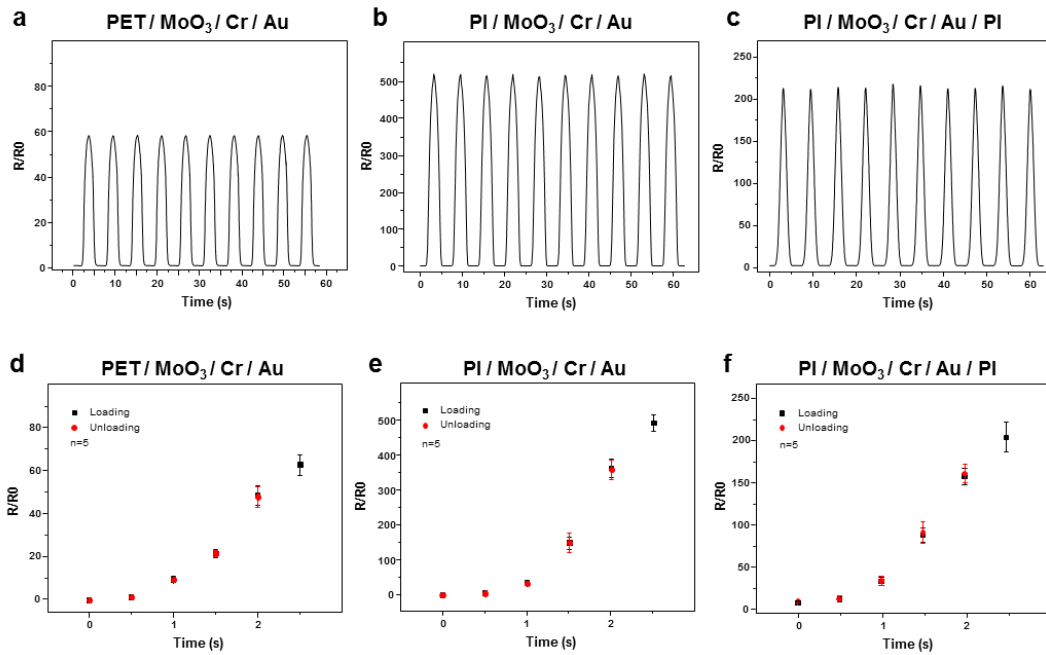


Figure 3-10. The normalized resistance variations of the crack sensors with strain. (a) The normalized resistance variance versus 2% strain in 10 times cyclic test of the crack sensor on PET substrate. (b) The crack sensor on PI substrate without the encapsulating layer. (c) The crack sensor on PI substrate with the encapsulating layer. (d) Reproducible and hysteresis test obtained from crack sensors on PET substrate. (e) Crack sensors on PI substrate without the encapsulating layer. (f) The crack sensors on PI substrate with the encapsulating layer.

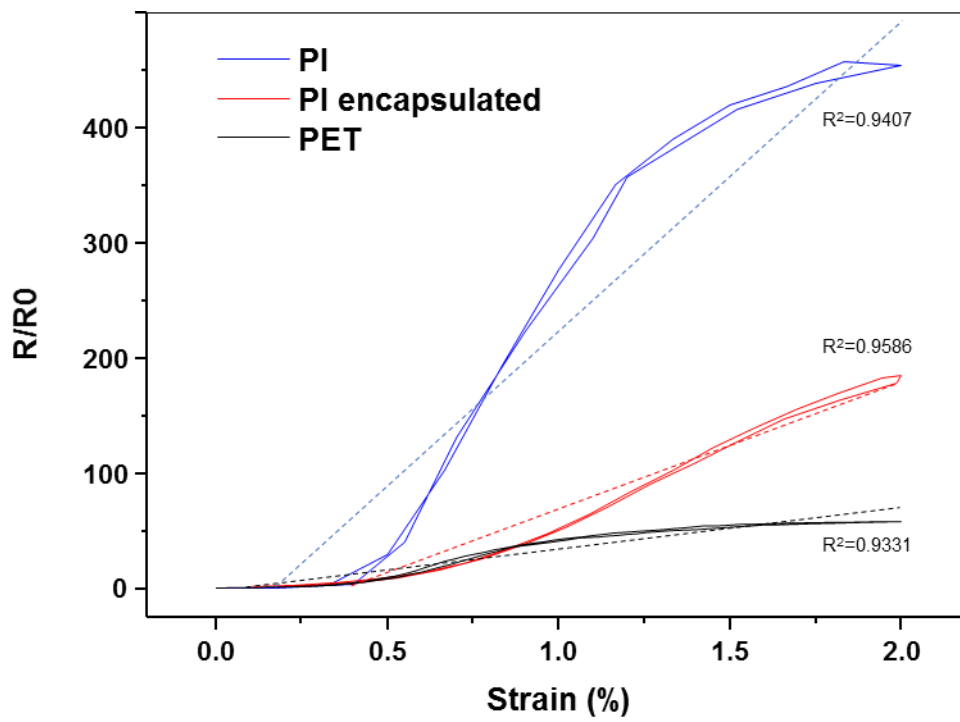


Figure 3-11. Strain-response curve of crack sensors.

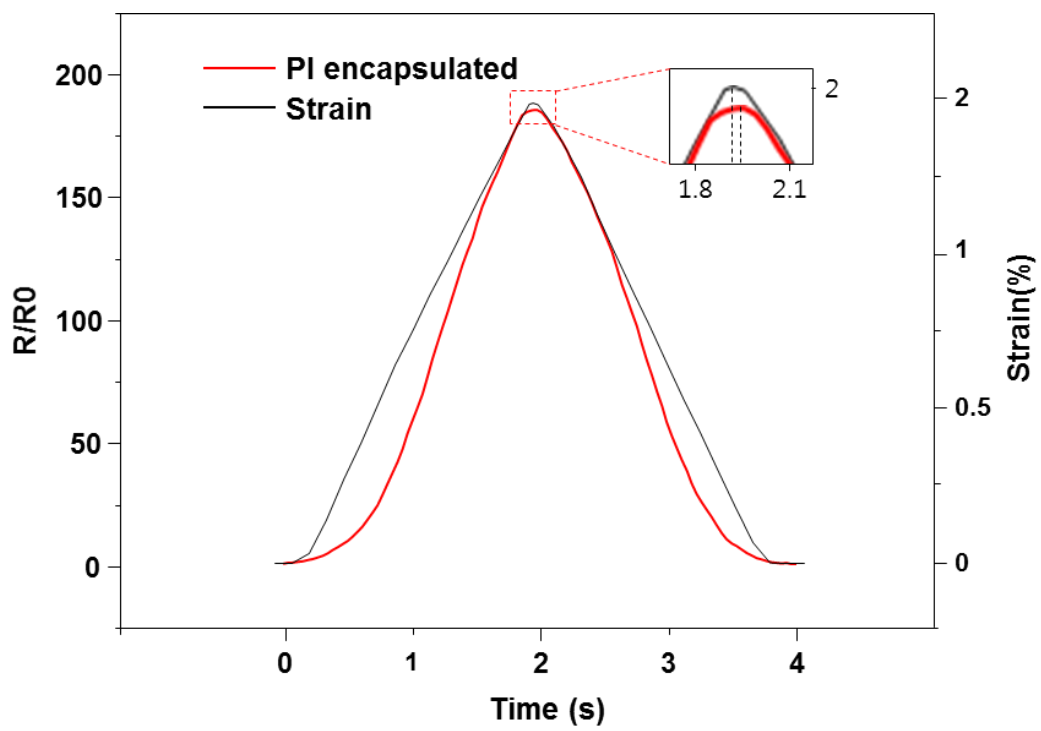


Figure 3-12. The response time of the encapsulated crack based sensor.

3-1-3-2. FEP Encapsulated crack sensors

Polyimide encapsulations stabilize the crack sensors with harsh environments such as water, chemical, and high temperature. However, slight degradation occurs when the constant water or chemical is enhanced on the encapsulated crack sensors. Thus, to improve stability of the crack sensors, we present FEP encapsulated crack sensors. The properties of FEP are similar to Polytetrafluorethylene (PTFE). FEP resists the chemical such as Acetic acid, water, and formic acid. [38] **Fig. 3-13** is the schematic image of fabrication of the FEP encapsulated crack sensor. The thickness of FEP films is 25 μm and 50 μm . Two holes are drilled by laser to contact the wire to the crack sensor. The glass transition temperature of the FEP film is about 70° C with pressure of 50 bar in a second. **Fig. 3-14** is the image of the FEP encapsulated crack sensor. We have stabilization tests under the water condition. The FEP encapsulated crack sensors maintain their performance in the presence of water. (**Fig. 3-15**) After the water test, the FEP encapsulated crack sensors are stretched 15,000 times strain from 0% to 2% for testing the durability of crack sensors. **Fig. 3-16** is the graph of durability test. It shows the FEP encapsulated crack sensors maintain their performance after 15,000 times cyclic test. **Fig. 3-17** is the durability graph comparing between the PI encapsulated crack sensors and the FEP encapsulated crack sensors. **Fig. 3-18** is the images of the FEP encapsulated crack sensors fail to resist water. When the sensors fail to resist water, the metal layers are peeled off from the substrates, PI. In the **Fig. 3-18**, the red dot circles indicate the area where

the metal layers are peeled off. As mentioned on **section 3-1-3-1**, the metal layers are peeled off rapidly when crack sensors face the water environment without encapsulation. This result shows the performance degradation of crack sensors. We have tested the water vapor permeability the **Table 3-1** is the water vapor permeability of the FEP films with thickness of 25 μm and 50 μm . The water vapor permeability is measured with temperature of 37.6 $^{\circ}\text{C}$, and flow rate is 9.92 SCCM ($= \text{cm}^3/\text{min}$). The water vapor permeability of the 50 μm FEP film is 2.06 $\text{g}/(\text{m}^2 \cdot \text{day})$ and the 25 μm FEP film is 4.65 $\text{g}/(\text{m}^2 \cdot \text{day})$. We have saline resist tests with NaCl 0.9% in 15 days. The FEP encapsulated crack sensors resist from saline about 15 days without losing their performances. (**Fig. 3-19**)

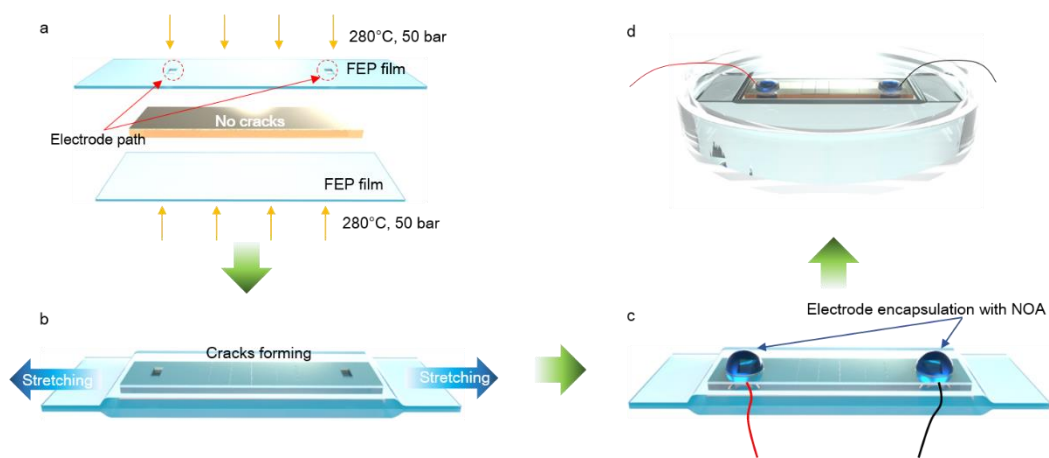


Figure 3-13. The schematic images of the FEP encapsulated crack sensor fabrication. (a) The metal layer deposited PI film is impressed in between the double FEP films by 280° C, 50 bar in a second. (b) After impressing, cracks are formed by stretch the FEP films.

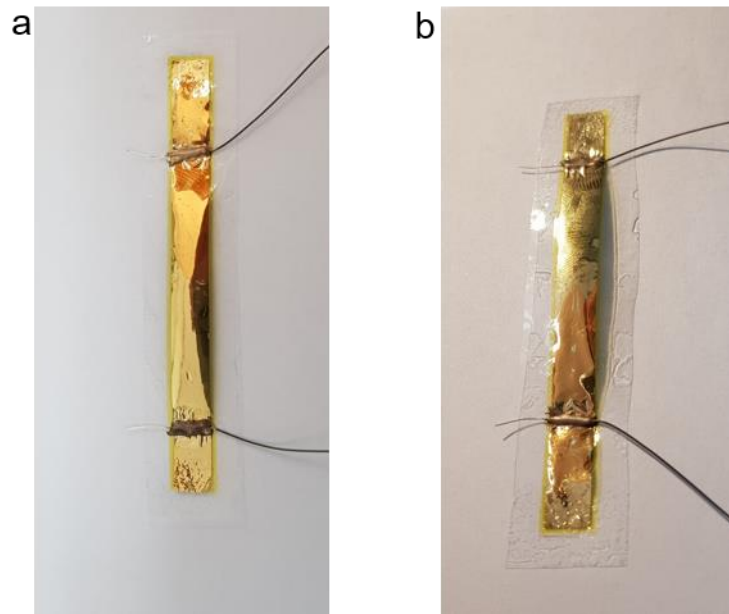


Figure 3-14. The image of the FEP encapsulated crack sensor (a) before water resist test, (b) after water resist test.

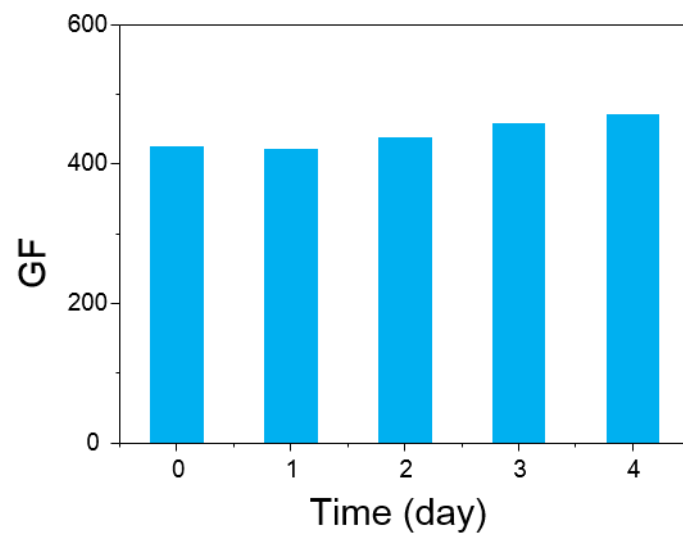


Figure 3-15. The graph of the FEP encapsulated crack sensor gauge factor varies with time in water.

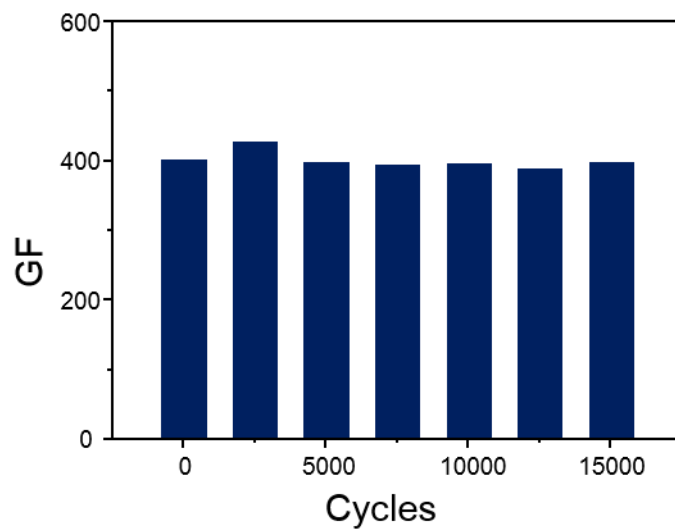


Figure 3-16. The durability test of the FEP encapsulated crack sensors after the water resist test.

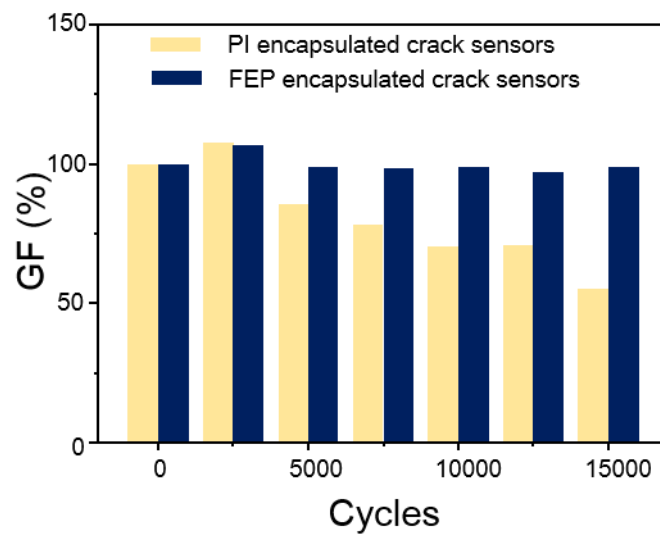


Figure 3-17. The durability comparison of the FEP encapsulated crack sensors (blue lines), and the PI encapsulated crack sensors (yellow lines).



Figure 3-18. The photo images of the FEP encapsulated crack sensors after water resist test. (a) No metal layers were peeled off from the PI substrate. (b) The metal layers on red dot area were peeled off from the PI substrate.

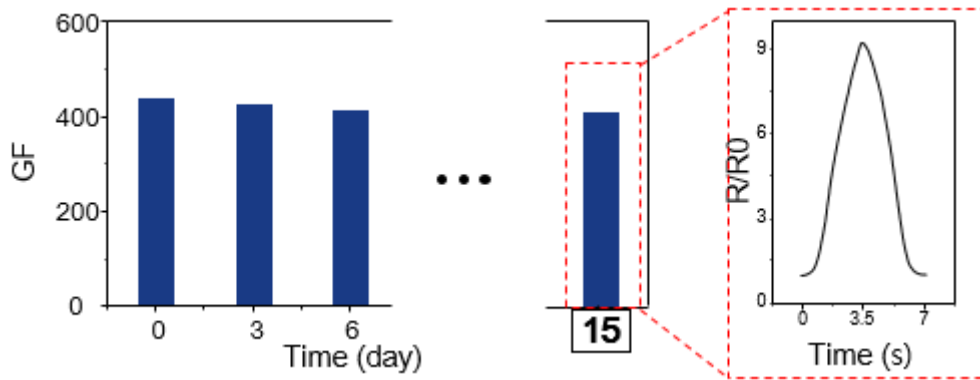


Figure 3-19. The saline resist test of the FEP encapsulated crack sensors. The encapsulated crack sensors withstand their performance until 15 days within saline conditions

Sample	Water vapor permeability (g/(m ² ·day))
25 um thickness of FEP film	2.06
50 um thickness of FEP film	4.65

Table 3-1. The water vapor permeability test of the FEP films.

3-1-4. Summary

We have demonstrated that the PI encapsulated crack sensor can operate in a harsh environment such as of hot, water, and saline solution. After deposition of MoO₃, Cr, and Au on the thin polyimide film, the crack was generated by stretching, and lastly, the sample was covered with a PI solution and cured on a hot plate. Several advantages of encapsulation of the crack sensor, which are thermal resistance, water/saline solution resistance, and durability were verified by experiments. The results represent that the thermal, water & saline solution resistances were improved by encapsulation. Concretely, the encapsulated sensor is heat-endurable even at 300 °C, water-resistible for 30 hours, and saline sloution-endurable for 24 hours with the gauge factor of 2 % strain. These results show its capability to be used as an wearable device and strain gauge at high temperature.

3-1-5. References

- [1] Kinkeldei, T., Munzenrieder, N., Zysset, C., Cherenack, K., Tröster, G. 2011, **32**, 1743-1745.
- [2] Kim, D.-H., Ghaffari, R., Lu, N., Rogers, J.A. *Annual review of biomedical engineering* 2012, **14**, 113-128.
- [3] Kim, D.-H., Lu, N., Ghaffari, R., Kim, Y.-S., Lee, S.P., Xu, L., Wu, J., Kim, R.-H., Song, J., Liu, Z. *Nature materials* 2011, **10**, 316.
- [4] Kim, D.-H., Lu, N., Huang, Y., Rogers, J.A. *MRS bulletin* 2012, **37**, 226-235.
- [5] Wagner, S., Bauer, S. *Mrs Bulletin* 2012, **37**, 207-213.
- [6] Choi, M.-C., Kim, Y., Ha, C.-S. *Progress in Polymer Science* 2008, **33**, 581-630.
- [7] Kim, D.H., Liu, Z., Kim, Y.S., Wu, J., Song, J., Kim, H.S., Huang, Y., Hwang, K.c., Zhang, Y., Rogers, J.A. *Small* 2009, **5**, 2841-2847.
- [8] Chung, H.J., Sulkin, M.S., Kim, J.S., Goudeseune, C., Chao, H.Y., Song, J.W., Yang, S.Y., Hsu, Y.Y., Ghaffari, R., Efimov, I.R. *Advanced healthcare materials* 2014, **3**, 59-68.
- [9] Xu, S., Zhang, Y., Jia, L., Mathewson, K.E., Jang, K.-I., Kim, J., Fu, H., Huang, X., Chava, P., Wang, R. *Science* 2014, **344**, 70-74.
- [10] Atalay, O., Atalay, A., Gafford, J., Wang, H., Wood, R., Walsh, C. *Advanced*

Materials Technologies 2017, **2**.

- [11] Lee, J., Kim, S., Lee, J., Yang, D., Park, B.C., Ryu, S., Park, I. *Nanoscale* 2014, **6**, 11932-11939.
- [12] Wang, Y., Wang, L., Yang, T., Li, X., Zang, X., Zhu, M., Wang, K., Wu, D., Zhu, H. *Advanced Functional Materials* 2014, **24**, 4666-4670.
- [13] Kang, D., Pikhitsa, P.V., Choi, Y.W., Lee, C., Shin, S.S., Piao, L., Park, B., Suh, K.-Y., Kim, T.-i., Choi, M. *Nature* 2014, **516**, 222-226.
- [14] Choi, Y.W., Kang, D., Pikhitsa, P.V., Lee, T., Kim, S.M., Lee, G., Tahk, D., Choi, M. *Scientific reports* 2017, **7**.
- [15] Lee, T., Choi, Y.W., Lee, G., Pikhitsa, P.V., Kang, D., Kim, S.M., Choi, M. *Journal of Materials Chemistry C* 2016, **4**, 9947-9953.
- [16] Park, B., Kim, J., Kang, D., Jeong, C., Kim, K.S., Kim, J.U., Yoo, P.J., Kim, T.i. *Advanced Materials* 2016, **28**, 8130-8137.
- [17] WhanáChoi, Y., MoonáKim, S. *RSC Advances* 2017, **7**, 34810-34815.
- [18] van den Brand, J., De Kok, M., Koetse, M., Cauwe, M., Verplancke, R., Bossuyt, F., Jablonski, M., Vanfleteren, J. *Solid-State Electronics* 2015, **113**, 116-120.
- [19] Takei, K., Takahashi, T., Ho, J.C., Ko, H., Gillies, A.G., Leu, P.W., Fearing, R.S., Javey, A. *Nature materials* 2010, **9**, 821.
- [20] Viventi, J., Kim, D.-H., Vigeland, L., Frechette, E.S., Blanco, J.A., Kim, Y.-S., Avrin, A.E., Tiruvadi, V.R., Hwang, S.-W., Vanleer, A.C. *Nature*

- neuroscience* 2011, **14**, 1599-1605.
- [21] Viventi, J., Kim, D.-H., Moss, J.D., Kim, Y.-S., Blanco, J.A., Annetta, N., Hicks, A., Xiao, J., Huang, Y., Callans, D.J. *Science translational medicine* 2010, **2**, 24ra22-24ra22.
- [22] Byun, I., Coleman, A.W., Kim, B. *Journal of Micromechanics and Microengineering* 2013, **23**, 085016.
- [23] Dauskardt, R., Lane, M., Ma, Q., Krishna, N. *Engineering Fracture Mechanics* 1998, **61**, 141-162.
- [24] Waters, P., Volinsky, A. *Experimental mechanics* 2007, **47**, 163-170.
- [25] Alaca, B.E., Saif, M., Sehitoglu, H. *Acta Materialia* 2002, **50**, 1197-1209.
- [26] Yu, H.-H., He, M., Hutchinson, J. *Acta materialia* 2001, **49**, 93-107.
- [27] Miller, R.A., Lowell, C.E. *Thin solid films* 1982, **95**, 265-273.
- [28] Wiklund, U., Gunnars, J., Hogmark, S. *Wear* 1999, **232**, 262-269.
- [29] Evans, A., He, M., Hutchinson, J. *Progress in Materials Science* 2001, **46**, 249-271.
- [30] Evans, A., Hutchinson, J. *Surface and Coatings Technology* 2007, **201**, 7905-7916.
- [31] Hutchinson, J., Evans, A. *Surface and Coatings Technology* 2002, **149**, 179-184.
- [32] Leung, S.Y., Lam, D.C.C., Luo, S., Wong, C. *Journal of adhesion science and technology* 2004, **18**, 1103-1121.

- [33] Martena, M., Botto, D., Fino, P., Sabbadini, S., Gola, M., Badini, C. *Engineering Failure Analysis* 2006, **13**, 409-426.
- [34] Koros, W., Paul, D. *Journal of Polymer Science Part B: Polymer Physics* 1978, **16**, 2171-2187.
- [35] Groeninckx, G., Reynaers, H., Berghmans, H., Smets, G. *Journal of Polymer Science Part B: Polymer Physics* 1980, **18**, 1311-1324.
- [36] Ghosh, M. *Polyimides: Fundamentals and applications*. CRC Press: 1996.
- [37] Park, B., Lee, S., Choi, H., Kim, J.U., Hong, H., Jeong, C., Kang, D., Kim, T.-i. *Nanoscale* 2018.
- [38] Wang, H., Liu, Z., Wang, E., Zhang, X., Yuan, R., Wu, S., Zhu, Y., *Applied Surface Science*, 2015, **357**, 229-235.

Acknowledgement

This work was funded by the Global Frontier R&D program on Center for Multiscale Energy System by the National Research Foundation under the Ministry of Science, ICT, and Future Planning, Korea.

The results of chapter 2, 'Brittle thin layer induced diverse conductive materials layered crack-based sensory systems' are collaborated with Yong Whan Choi (Seoul National University, February 2017).

국 문 초 록

본 논문은 금속 박막의 상이한 파단 특성을 이용한 다중 금속 박막 구조의 파단 기반 미세 변화 감지 센서와 고분자의 열 변형 성질 기반 붕지 기술이 접목된 내구성이 우수한 미세 변화 감지 센서를 제시하였다.

먼저, 가해지는 인장에 대한 상이한 금속 박막의 파단 형성 특성을 이용하여 새롭고, 제작이 용이한 파단 기반 미세 변화 감지 센서에 대해 소개하였다. 파단 기반 미세 변화 감지 센서의 파단 형성을 위해 취성이 있는 금속 박막과 전도성이 우수한 금속 박막을 결합하여 전도성 박막에 파단이 인가하였다. 파단이 인가된 전도성 박막은 연신에 대해 높은 저항변화를 갖는다. 또한 접착력이 있는 옥사이드 박막을 파단 형성 금속 박막과 지지대 사이에 증착하여, 반복 하중에 안정성을 갖는 센서를 구현하였다.

다음으로, 취성 있는 투명 전도성 박막에 인가된 파단 기반 미세 변화 감지 센서의 연구를 제시하였다. 가시광선 영역에서 높은 투과도, 우수한 전도도, 그리고 작은 연신에 파단을 형성 하는 인듐 주석 산화물은 투명한 파단 기반 미세 변화 감지 센서로 적합하다. 따라서, 인듐 주석 산화물을 투명하고 연신이 가능한 고분자 지지대에 증착 한 후 연신을 가해 파단을 인듐 주석 산화물에 인가하는 단순한 제작 공법을 통해 투명한 파단 기반 미세 변화 감지 센서를 구현하였다.

제시한 감지 센서는 미세 연신에 대한 높은 민감도, 가시 광선에 대한 높은 투과도, 그리고 반복 연신에 대한 안정된 특성을 갖는다. 추가로, 연신에 대한 파단 변화 특성을 활용하여 압력을 측정 하는 투명 미세 압력 감지 센서를 개발하였다. 개발된 투명 압력 센서 또한 압력에 높은 민감도, 넓은 압력 측정 범위, 가시광선에 대한 높은 투과도를 갖는다.

다음으로, 고분자의 열 변형 특성을 통한 파단 기반 미세 변화 감지 센서의 안정화 방안을 제시하였다. 기존의 파단 기반 센서의 경우, 표면 금속 박막이 직접 외부로 노출되어 있어 외부의 극한 환경에 취약하다. 본 연구에서는 내 화학성과 투습도가 낮은 고분자를 이용하여 파단이 형성된 금속 박막을 외부로부터 보호하여 센서의 내구성의 증대를 도모하였다.

주요어: 다층 박막 구조, 금속 박막 파단, 연신 측정, 압력 측정, 봉지 기술

학번: 2014-31037